

Plastic scintillation dosimetry for radiation therapy: minimizing capture of Cerenkov radiation noise

This content has been downloaded from IOPscience. Please scroll down to see the full text.

2004 Phys. Med. Biol. 49 783

(<http://iopscience.iop.org/0031-9155/49/5/009>)

View [the table of contents for this issue](#), or go to the [journal homepage](#) for more

Download details:

IP Address: 134.99.128.41

This content was downloaded on 08/01/2014 at 14:18

Please note that [terms and conditions apply](#).

Plastic scintillation dosimetry for radiation therapy: minimizing capture of Cerenkov radiation noise

A Sam Beddar¹, Natalka Suchowerska² and Susan H Law³

¹ Department of Radiation Physics, Division of Radiation Oncology, University of Texas, M D Anderson Cancer Center, Houston, TX, USA

² Department of Radiation Oncology, Royal Prince Alfred Hospital and University of Sydney, NSW, Australia

³ Australian Photonics CRC/Optical Fibre Technology Centre, University of Sydney, NSW, Australia

Received 15 October 2003

Published 13 February 2004

Online at stacks.iop.org/PMB/49/783 (DOI: 10.1088/0031-9155/49/5/009)

Abstract

Over the last decade, there has been an increased interest in scintillation dosimetry using small water-equivalent plastic scintillators, because of their favourable characteristics when compared with other more commonly used detector systems. Although plastic scintillators have been shown to have many desirable dosimetric properties, as yet there is no successful commercial detector system of this type available for routine clinical use in radiation oncology. The main factor preventing this new technology from realizing its full potential in commercial applications is the maximization of signal coupling efficiency and the minimization of noise capture. A principal constituent of noise is Cerenkov radiation. This study reports the calculated capture of Cerenkov radiation by an optical fibre in the special case where the radiation is generated by a relativistic particle on the fibre axis and the fibre axis is parallel to the Cerenkov cone. The fraction of radiation captured is calculated as a function of the fibre core refractive index and the refractive index difference between the core and the cladding of the fibre for relativistic particles. This is then used to deduce the relative intensity captured for a range of fibre core refractive indices and fibre core–cladding refractive index differences. It is shown that the core refractive index has little effect on the amount of radiation captured compared to the refractive index difference. The implications of this result for the design of radiation therapy plastic scintillation dosimeters are considered.

(Some figures in this article are in colour only in the electronic version)

1. Introduction

The rapid development of technically sophisticated radiation therapy beam delivery techniques has driven the demand for appropriate dosimetry. Time-dependent techniques (e.g. intensity-

modulated radiation therapy (IMRT)) and precision techniques (e.g. stereotactic radiosurgery) potentially deliver improved therapeutic results with reduced morbidity. However, confidence in these techniques is often restrained due to the lack of *in vivo* dosimeters with both high spatial and high temporal resolution, preferably supplying dosimetric data in real time. The primary difficulty with current dosimeters is their size (Beddar *et al* 2001), which limits both their spatial resolution and the feasibility of their use in confined *in vivo* situations. This limitation may be overcome by the use of miniature plastic scintillators coupled to a detector via an optical fibre (Beddar *et al* 1992a, 1992b). As discussed by Beddar *et al* (2003) the broad range of application of this technique can be limited by the signal-to-noise ratio.

To date the signal levels from such dosimeters have been limited by the coupling between the scintillator and the fibre (Beddar *et al* 2003). This can be improved by the concurrent engineering of scintillator/fibre coupling techniques and optimized fibre design. Ultimately, the coupling of scintillator light into the fibre will be constrained by the core size and the numerical aperture of the fibre. Since the bulk of the noise is due to capture of light photons generated within the fibre core (Cerenkov radiation, fluorescence and luminescence) both core size and numerical aperture of the fibre will also affect the noise level on the signal. As obvious factors that increase signal will also increase noise, a thorough understanding of the capture processes is essential to discriminate against the initial capture of noise, thereby effectively optimizing the fibre design for this type of application: scintillation dosimetry.

This preliminary study will concentrate on the capture of Cerenkov radiation for two reasons. The first is that Cerenkov noise is the predominant and therefore the most significant noise generating process in plastic scintillation dosimetry (Beddar *et al* 1992c). The second is that a discriminating characteristic of Cerenkov radiation is its emission around a cone at a preferential angle (the Cerenkov angle). This anisotropic distribution in the propagation direction of the light means that trapping of light by the coupling fibre will be a function of the angle between the particle track and the fibre axis.

2. Origins of Cerenkov radiation

Cerenkov radiation is generated when a particle travels through a medium at speeds greater than the local speed of light (c/n where c is the speed of light in vacuum and n is the refractive index of the medium) (Richtmyer *et al* 1969). Such a particle generates a cone of light spreading out at the Cerenkov angle, $\kappa = \arccos(1/n\beta)$, where β is the ratio of the speed of the particle (v) to the speed of light in vacuum (c). The intensity of this radiation, I , produced by a given electron flux density is proportional to $1 - (1/n^2\beta^2)$. From this it would appear that fibres with lower refractive index cores, n , would capture less Cerenkov radiation simply because less radiation is generated by the particles as they move through the core.

With an increase in particle energy, the particle velocity becomes relativistic and β asymptotically approaches unity. In this limit the Cerenkov angle is solely a function of the refractive index of the medium,

$$\kappa = \arccos(1/n) \quad (1)$$

and likewise the expression for the Cerenkov light intensity, I , becomes

$$I \propto 1 - (1/n^2). \quad (2)$$

Thus when a relativistic particle is passing through the fibre core it will generate a cone of light at an angle determined by the refractive index of the core. The intensity of that light is inversely dependent on the refractive index squared. However, not all the cone of radiation will necessarily be captured.

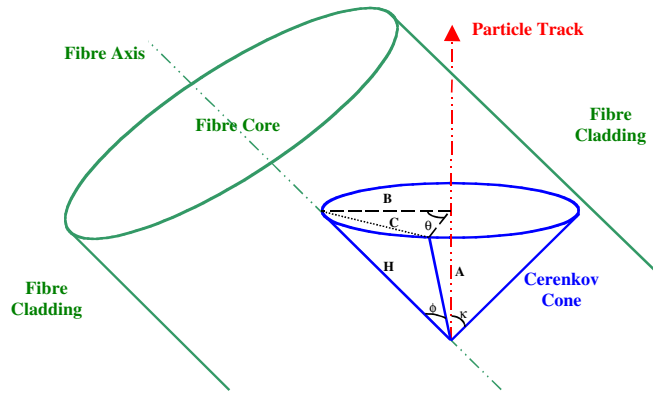


Figure 1. The geometry for the capture of Cerenkov radiation from a relativistic particle on the axis of an optical fibre in the case where the fibre axis lies along the Cerenkov cone.

In this paper we will look at the simplest case for the capture of Cerenkov radiation: a cone generated by a particle on the fibre axis with the fibre axis lying along one side of the cone. We will then use this to obtain a first approximation to the relationship between fibre parameters and the capture of Cerenkov radiation. We will then assess the balance between the fibre design for Cerenkov radiation elimination and the fibre design for maximizing the coupling of scintillation from a probe tip.

3. Theory

Figure 1 shows the geometry of the simplest case for the capture of Cerenkov radiation by the core of a waveguiding fibre. In this case the angle between the fibre axis and the particle track is equal to the Cerenkov angle and the radiation is emitted just as the travelling electron crosses the fibre axis. The origin of the Cerenkov cone thus lies upon the fibre axis.

The Cerenkov radiation is emitted in a cone of radiation at an angle κ , and the optical axis lies along the surface of the cone. In this case all the rays are meridional, i.e. pass through the fibre axis, and hence will be either bound or refracting (Snyder and Love 1983). Whether a ray is bound or refracting will be determined by its angle relative to the surface of the fibre core in its plane of propagation (its *propagating angle*). A ray will be bound (that is trapped by the fibre) if its propagating angle is less than the critical propagating angle of the fibre, which is defined as the complement of the critical angle of the core–cladding interface (as given by Snell's law). The ray that lies along the fibre axis has a propagating angle of 0° and will, of course, be bound.

Consider a ray at angle θ around the cone from the axial ray. From the geometry of the situation it is clear that the propagating angle of this ray is the angle, ϕ in the apex of the isosceles triangle formed by the ray at θ , the ray along the fibre axis, and the chord between the ends of the two rays. Using simple trigonometry we can derive an expression for the angle ϕ as follows.

For a given distance from the origin of the cone, A , the radius of the cone 'base', B , the ray length of the cone, H and C , the length of the chord between the axial ray and the ray at angle θ , are given by (figure 1)

$$\begin{aligned} B &= A \tan(\kappa) \\ H &= A / \cos(\kappa) \\ C &= 2B \sin(\theta/2) = 2A \tan(\kappa) \sin(\theta/2) \end{aligned} \quad (3)$$

where κ is the Cerenkov angle for the fibre core material. Drawing the perpendicular from the chord, C , to the apex at ϕ produces a pair of right angle triangles. Since the original triangle was isosceles, the perpendicular will bisect both the chord, C , and the angle, ϕ . The hypotenuse of these triangles is the ray length, H , so

$$\sin \frac{\phi}{2} = \frac{C/2}{H}.$$

Substituting equations (3) we obtain

$$\sin(\phi/2) = \sin(\kappa) \sin(\theta/2). \quad (4)$$

Since they are originating from a point on the fibre axis, all these rays are meridional, and will be bound if ϕ is less than the critical propagating angle, ϕ_c , given by

$$\cos(\phi_c) = n_{cl}/n_{co} \quad (5)$$

where n_{cl} and n_{co} are the cladding and core refractive indices of the fibre. If we define θ_B to be the angle around the cone such that the propagating angle of the Cerenkov ray is equal to the critical propagating angle of the fibre, then

$$\sin(\phi_c/2) = \sin(\kappa) \sin(\theta_B/2)$$

and the rays will be bound for all $\theta < \theta_B$.

By the trigonometric half-angle rule

$$\sin^2(\phi_c/2) = \frac{1}{2}(1 - \cos \phi_c)$$

and noting also that

$$\sin^2(\kappa) = 1 - \cos^2(\kappa)$$

we obtain

$$\frac{1}{2}(1 - \cos \phi_c) = (1 - \cos^2(\kappa)) \sin^2(\theta_B/2). \quad (6)$$

Substituting (1) and (5) into (6) and noting that $n_{co} - n_{cl} = \Delta n$ gives

$$\theta_B = 2 \arcsin \left(\sqrt{\frac{n_{co} \Delta n}{2(n_{co}^2 - 1)}} \right). \quad (7)$$

Thus for angles in the range $-\theta_B < \theta < \theta_B$ the rays of the Cerenkov cone are bound. Therefore the fraction of the Cerenkov cone captured by the fibre core is

$$\frac{2\theta_B}{2\pi} = \frac{\theta_B}{\pi} = \frac{2}{\pi} \arcsin \left(\sqrt{\frac{n_{co} \Delta n}{2(n_{co}^2 - 1)}} \right). \quad (8)$$

The captured intensity, I_c , will then be proportional to the product of equations (2) and (8):

$$I_c \propto \frac{2}{\pi} \arcsin \left(\sqrt{\frac{n_{co} \Delta n}{2(n_{co}^2 - 1)}} \right) \times \left(1 - \frac{1}{n_{co}^2} \right). \quad (9)$$

Thus for the case considered and for relativistic particles both the fraction of the cone captured and the captured intensity are functions solely of the fibre parameters n_{co} and Δn .

These two parameters are also critical in determining the amount of scintillation signal, which will couple into the fibre. Given a fibre with core refractive index n_{co} , index step Δn and core diameter d_c and a short scintillating probe of refractive index n_s , diameter D_s and length L_s (figure 2) then the volume from which generated scintillation can couple into the

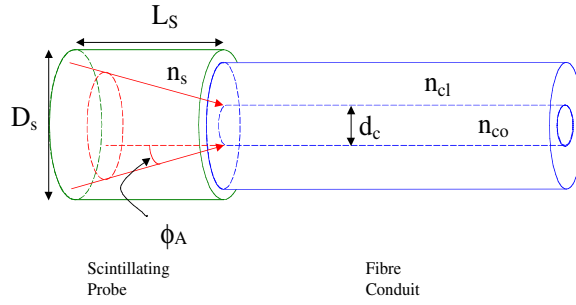


Figure 2. Geometry of the scintillation collection volume in a polymer probe tip.

fibre is a truncated cone expanding from the fibre core given by

$$V_{\text{coll}} = \pi L_s \left(\frac{d_c^2}{4} + L_s^2 \tan^2 \phi_A \right) \quad (10)$$

where ϕ_A is the acceptance angle of the fibre from the scintillator, which is given by

$$\sin \phi_A = \frac{n_{\text{co}}}{n_s} \sin \phi_c = \frac{\sqrt{2n_{\text{co}}\Delta n - \Delta n^2}}{n_s} \quad (11)$$

from the standard form of Snell's law and by substituting equation (5).

4. Results

The percentage of the Cerenkov cone captured and the relative intensity of Cerenkov radiation captured were calculated for fibre core refractive indices from 1.30 to 1.74, indices typical of optical glasses and plastics, and for core/cladding refractive index differences from 0.002 to 0.03. Figure 3 shows the fraction of the Cerenkov cone captured as a function of the fibre core refractive index and the refractive index difference of the fibre (Δn).

Although the effect is not as marked, the fraction of the Cerenkov cone captured decreases as the core refractive index increases. This is due to the widening of the cone angle as the refractive index increases. Not surprisingly, the fraction of the cone captured is extremely sensitive to refractive index difference (Δn), since this determines the critical angle for coupling of the signal into the fibre core.

Figure 4 shows the relative light intensity captured. As for the fraction of the Cerenkov cone captured, the relative intensity is strongly dependent on the core/cladding refractive index difference, increasing by a factor of 4 to 5 over the range of Δn considered. In contrast to the fraction of the cone captured (figure 3), the captured intensity (figure 4) increases with increasing core refractive index, the effect of the widening cone being more than compensated for by the increased intensity of the light generation.

5. Discussion

This study of the simplest case of Cerenkov radiation capture identifies important issues for the design of a plastic scintillation radiation dosimeter system. The intensity captured seems relatively insensitive to the refractive index of the core (though there may be an effective increase in the number of generating particles as the refractive index increases), but is strongly dependent on the difference of the refractive index between the fibre core and the fibre cladding.

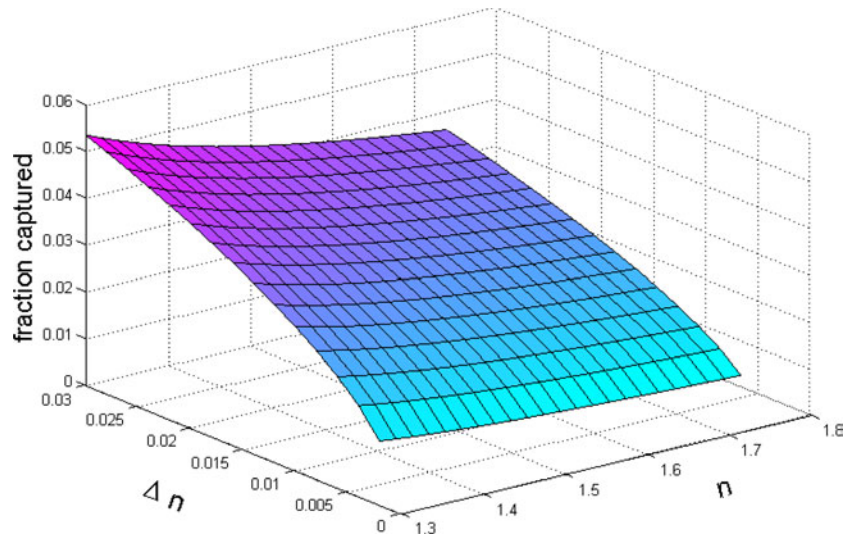


Figure 3. Fraction of Cerenkov cone captured as a function of refractive index and refractive index difference.

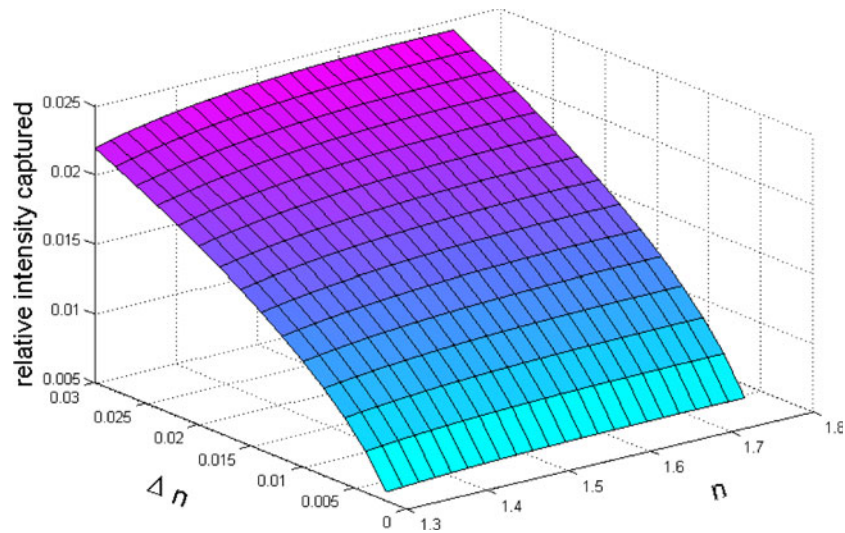


Figure 4. Relative intensity captured as a function of core refractive index and core/cladding difference.

To reduce the capture of Cerenkov radiation noise for this specific case, the core/cladding refractive index difference should be kept to a minimum. Unfortunately this reduces the acceptance angle of the fibre, and thus the volume of the scintillator probe from which the light can be collected (as can be seen from equation (10)). The collection volume will increase if the fibre core size is increased, but this will increase the fibre core volume, and thus increase the amount of Cerenkov radiation generated in the core.

The relative insensitivity of the noise level to the fibre core refractive index does raise another possible avenue for improving the scintillation gathering power of the system. As

equation (11) shows, $\sin \phi_A$ is proportional to the ratio of the core refractive index to the scintillator refractive index. If a high index material can be found for the fibre, and a low index material for the scintillator then the scintillation collection efficiency of the system will again be improved.

Future work will extend this analysis first to the case of an on-axis particle, but where the fibre axis does not lie on the Cerenkov cone. All the rays will still be meridional, simplifying the boundary condition for coupling and thus the calculation of the fraction of the Cerenkov cone trapped by the fibre. This will provide insight into the behaviour of the noise as a function of beam/fibre angle. Secondly the case of off-axis generation will be considered. This is considerably more complex than the first two cases as the beams can be either meridional or skew (Snyder and Love 1983) and the issue of leaky modes arises.

The implication of these results on plastic scintillation dosimetry for radiation therapy is that by improving our understanding of the signal and noise capture processes, we are better able to optimize this dosimeter design for general clinical application or for specific clinical procedures, as required.

6. Conclusion

Effective clinical utilization of plastic scintillation dosimeters is dependent on establishing optimal signal efficiency and minimizing noise. This is a preliminary study of optical variables governing the capture of Cerenkov radiation noise, providing insight into favourable design characteristics of plastic scintillation dosimeters in order to enhance signal-to-noise ratio.

Acknowledgments

The authors would like to acknowledge the support of their institutions and the encouragement of their colleagues at M D Anderson Cancer Center, the Royal Prince Alfred Hospital and the Optical Fibre Technology Centre at the University of Sydney.

Appendix. Ray optics terminology and waveguides

Having been developed to describe the propagation of rays of light through interfaces at near normal angles, Snell's law is traditionally defined in terms of deviation from the normal:

$$\frac{\sin \theta_1}{\sin \theta_2} = \frac{n_2}{n_1}.$$

This definition is awkward when working with optical waveguides where the light propagates nearly parallel to the interface, and in these cases Snell's law is defined in terms of the complementary 'propagating' angle, $\phi = 90 - \theta$, in which case

$$\frac{\cos \phi_1}{\cos \phi_2} = \frac{n_2}{n_1}.$$

At the end of the fibre, however, this 'propagating' angle is equal to the deviation from the normal for the refraction of light out of or into the fibre.

References

- Beddar A S, Kinsella T J, Ikhlef A and Sibata C H 2001 A miniature 'scintillator-fiberoptic-PMT' detector system for the dosimetry of small fields in stereotactic radiosurgery *IEEE Trans. Nucl. Sci.* **48** 924–8

- Beddar A S, Law S H, Suchowerska N and Mackie T R 2003 Plastic scintillation dosimetry: optimisation of light collection efficiency *Phys. Med. Biol.* **48** 1141–52
- Beddar A S, Mackie T R and Attix F H 1992a Water-equivalent plastic scintillation detectors for high-energy beam dosimetry: I. Physical characteristics and theoretical considerations *Phys. Med. Biol.* **37** 1883–900
- Beddar A S, Mackie T R and Attix F H 1992b Water-equivalent plastic scintillation detectors for high-energy beam dosimetry: II. Properties and measurements *Phys. Med. Biol.* **37** 1901–13
- Beddar A S, Mackie T R and Attix F H 1992c Cerenkov light generated in optical fibres and other light pipes irradiated by electron beams *Phys. Med. Biol.* **37** 925–35
- Richtmyer F K, Kennard E H and Cooper J N 1969 *Introduction to Modern Physics* (New York: McGraw-Hill)
- Snyder A W and Love J D 1983 *Optical Waveguide Theory* (London: Chapman and Hall)

Monte Carlo study of the energy and angular dependence of the response of plastic scintillation detectors in photon beams

Lilie L. W. Wang, David Klein, and A. Sam Beddar^{a)}

Department of Radiation Physics, The University of Texas M. D. Anderson Cancer Center, Houston, Texas 77030

(Received 17 November 2009; revised 16 August 2010; accepted for publication 17 August 2010; published 17 September 2010)

Purpose: By using Monte Carlo simulations, the authors investigated the energy and angular dependence of the response of plastic scintillation detectors (PSDs) in photon beams.

Methods: Three PSDs were modeled in this study: A plastic scintillator (BC-400) and a scintillating fiber (BCF-12), both attached by a plastic-core optical fiber stem, and a plastic scintillator (BC-400) attached by an air-core optical fiber stem with a silica tube coated with silver. The authors then calculated, with low statistical uncertainty, the energy and angular dependences of the PSDs' responses in a water phantom. For energy dependence, the response of the detectors is calculated as the detector dose per unit water dose. The perturbation caused by the optical fiber stem connected to the PSD to guide the optical light to a photodetector was studied in simulations using different optical fiber materials.

Results: For the energy dependence of the PSDs in photon beams, the PSDs with plastic-core fiber have excellent energy independence within about 0.5% at photon energies ranging from 300 keV (monoenergetic) to 18 MV (linac beam). The PSD with an air-core optical fiber with a silica tube also has good energy independence within 1% in the same photon energy range. For the angular dependence, the relative response of all the three modeled PSDs is within 2% for all the angles in a 6 MV photon beam. This is also true in a 300 keV monoenergetic photon beam for PSDs with plastic-core fiber. For the PSD with an air-core fiber with a silica tube in the 300 keV beam, the relative response varies within 1% for most of the angles, except in the case when the fiber stem is pointing right to the radiation source in which case the PSD may over-respond by more than 10%.

Conclusions: At $\pm 1\%$ level, no beam energy correction is necessary for the response of all three PSDs modeled in this study in the photon energy ranges from 200 keV (monoenergetic) to 18 MV (linac beam). The PSD would be even closer to water equivalent if there is a silica tube around the sensitive volume. The angular dependence of the response of the three PSDs in a 6 MV photon beam is not of concern at 2% level. © 2010 American Association of Physicists in Medicine. [DOI: 10.1118/1.3488904]

Key words: plastic scintillation detector, energy dependence, angular dependence, Monte Carlo

I. INTRODUCTION

Plastic scintillation detectors (PSDs) have many advantages for ionizing radiation dosimetry,¹⁻⁴ e.g., water equivalence, photon beam-quality independence, dose-rate independence, linearity with dose, instantaneous readout, and high spatial resolution. All these merits make PSDs preferable to other detectors for real-time *in vivo* dosimetry.^{3,5-7} PSDs are generally categorized as being one of two types.⁸ Those with cladding around the scintillating core are called *scintillating fibers* and those without it are called *plastic scintillators*. Scintillating fibers are recently developed PSDs. Their major merits are their small detector volume (roughly 1 mm³), which gives them high spatial resolution, and their cladding, which reduces the loss of optical photons. Plastic scintillators are traditional PSDs. They can be made into any size and shape and thus cladding is not used. For in-phantom dose measurements, such as percent-depth dose curves or dose profiles, the placement and orientation of PSDs are usually well controlled, thus the angular or directional dependence of PSDs are not of concern. For *in vivo* applications, however,

since it is difficult to control and ensure the orientation of the detectors relative to the radiation source (either external beams or brachytherapy sources), the angular dependence of PSDs could be an issue and needs to be investigated. This is especially true considering the presence of an optical fiber coupled to a PSD to guide the optical light to a photodetector. Angular dependence can be axial (e.g., for typical placement, the radiation beam axis is always perpendicular to the detector axis) or azimuthal (the angle between the beam axis and the detector axis varies). Axial dependence should not exist for PSDs because of their cylindrical symmetry. In this work, therefore, we investigated only azimuthal angular dependence. Only a few studies have been published on the angular dependence of PSD responses and they considered only low-energy photon beams, a diagnostic x-ray source,⁹ and a brachytherapy source.^{5,10} For the diagnostic x-ray source, the measurement was performed free-in-air for one revolution of a clinical computed tomography (CT) unit (operating at 120 kVp) around the detector. The signal was reduced dramatically when the radiation was incident from the

back of the PSD because of the attenuation of the x ray in the optical fiber.⁹ It is expected that the effect would be reduced for in-phantom measurements due to scattering effect. For the brachytherapy sources, the measurement was performed in a polymethylmethacrylate (PMMA) phantom with an ¹⁹²Ir high dose-rate brachytherapy source. It was found that the PSD's sensitivity varied by about 2% in the range of angles studied.⁵ Unfortunately, no data are available for back-incident situations; in particular, when the optical fiber stem points directly to the radiation source.

In this study, we used EGSnrc^{11,12} Monte Carlo codes to investigate the angular dependence of PSD responses in photon beams. Because it was previously demonstrated experimentally^{13,14} that the light yield from a PSD is proportional to the energy deposited for the range of energies considered here (>200 keV), we scored the absorbed dose in the detector and used the detector dose per unit phantom dose as a measure of the detector's response. In fact, a PSD's response is also dependent on such factors as the generating efficiency of the fluorescent light in the detector and the coupling efficiency between the PSD and optical fiber.^{15,16} We did not consider those factors in the current study because we were only interested in the relative dosimetry and these factors will not affect the results as long as they can be kept at a constant. Čerenkov radiation induced in the optical fiber by the incident radiation beam is an important issue with the PSD-based dosimetry.^{2,16,17} Various methods have been described to remove the Čerenkov radiation from the detector's signal.^{2,4,18–20} An elegant method of circumventing the production of Čerenkov radiation in the optical fiber has also been proposed.^{21,22} Since air has a refractive index very close to 1, those investigators used a hollow optical fiber (filled with air) instead of one with a solid fiber core to minimize the generation of Čerenkov radiation. In this work, we assumed the Čerenkov light was not present or was completely removed. As a first step, we studied the energy dependence (or beam-quality dependence) of PSDs in photon beams with low ($<0.3\%$, 1σ) statistical uncertainties and compared the results to those obtained using the Burlin cavity theory¹ and those calculated previously²³ (2%–4%, 1σ) using the MCNP (Ref. 24) Monte Carlo code. Next, we studied the angular dependence of PSDs and the perturbation effect of the optical fiber of different materials (plastic, glass, or air) on detector response.

II. MATERIALS AND METHODS

II.A. Computational models of PSDs

We modeled three PSDs based on the specifications of the commonly used BC-400 plastic scintillator and BCF-12 scintillating fiber (Saint-Gobain Crystals, Nemours, France). Figure 1 shows schematically the computational models for the two of the three modeled PSDs coupled to an optical fiber 3 cm long. The optical fiber modeled was the Eska Premier GH4001 (Mitsubishi Rayon Co. Ltd., Tokyo, Japan). Figure 1(a) shows the BC-400 plastic scintillator (model 1). The detector material is polyvinyltoluene (PVT) wrapped with polystyrene. The core of the optical fiber is PMMA which is

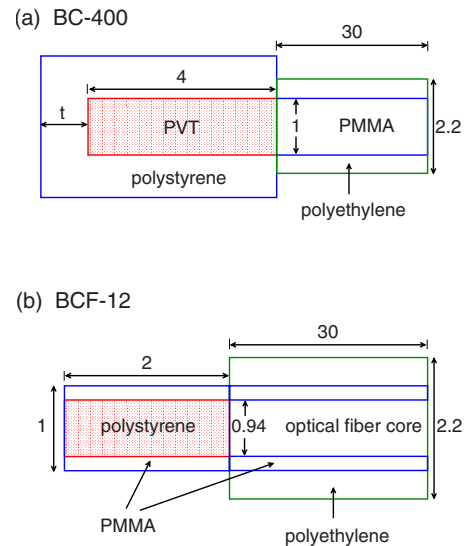


FIG. 1. Computational models of two PSDs for (a) BC-400, which uses PVT as the sensitive material, and (b) BCF-12, which uses polystyrene doped with fluor as the sensitive material. The sensitive region is designated by the shaded area. All measures are in millimeters. For BC-400, the polystyrene thickness at the tip of the PVT is either 3 or 1 mm.

protected by a polyethylene jacket. No cladding is used for this scintillator and so no cladding was modeled for the attached optical fiber. The thickness of the polystyrene on the tip of the PVT detector was modeled at 1 mm in this study. Figure 1(b) shows the BCF-12 scintillating fiber (model 2), in which the sensitive material is polystyrene doped with fluor. A PMMA cladding 30 μm thick was modeled for both the scintillating fiber and the optical fiber. Also modeled was a polyethylene jacket outside of the optical fiber. The optical fiber core of the scintillating fiber is PMMA. To see how the optical fiber core material affects, if any, the response of the PSD, we replaced the PMMA core with either silica (or glass, SiO_2) or air and calculated the responses of the PSDs. With a glass-core fiber of diameter of 1 mm, we simulate the Ft-1.0-UMT quartz optical fiber made by 3M (3M Canada, London, Ontario, Canada). The glass-core fiber was used in scintillator dosimetry²⁵ because it has high light transmission efficiency. Air has also been used as a core material for optical fibers²¹ to circumvent the generation of Čerenkov light. Naseri *et al.*²² studied experimentally and computationally the interdosimeter effect of an array of BC-400 scintillators with air-core optical fiber with a glass tube. Since a simple replacement of PMMA core by air does not correspond to the realistic air-core optical fiber, we also modeled this scintillator with air-core fiber as in Fig. 2, which is our third model (model 3), with the geometrical data taken from Naseri *et al.*,²² except we used polystyrene as the material for the black polymer sheath.

II.B. Energy cutoff and other Monte Carlo parameters

As there exists a very thin structure, e.g., silver layer of 0.12 μm , in the model of the air-core fiber with a silica tube (Fig. 2), the electron transport cutoff could be an issue in the Monte Carlo simulation. The generally used energy cutoff

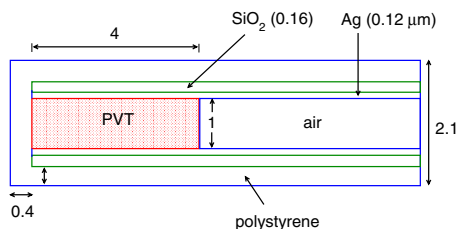


FIG. 2. Computational model of a BC-400 scintillator, which was used by Naseri *et al.* (Ref. 22), with air-core optical fiber with a silica tube. The sensitive region is designated by the shaded area. All measures are in millimeters unless specified.

for electron (ECUT) and energy cutoff for photon (PCUT) transports in EGSnrc is 521 keV (or 10 keV kinetic energy) and 10 keV, respectively. The 10 keV electron kinetic energy corresponds to a continuous slowing down approximation range of electrons in silver of $0.56 \mu\text{m}$, larger than the silver layer thickness in the model. To increase the spatial resolution, a lower energy cutoff should be used and this would lead to a longer simulation time. We have compared the calculated dose in the scintillator for different particle energy cutoffs for three orientations of the scintillator at 10 cm depth in a 6 MV photon beam. The results are shown in Table I, where the dose is normalized to that calculated with ECUT=512 keV and PCUT=1 keV. The results suggest that for this particular model, the difference in detector doses by using different energy cutoffs is negligible at about 0.2% level. For this reason, we used 521 keV for electron cutoff and 10 keV for photon cutoff in this study, which takes roughly only one third of calculation time than when 512 keV and 1 keV are used. The detector dose was scored in the sensitive region of the scintillators (shaded areas in Figs. 1 and 2). The phantom dose was scored in a disk voxel with a diameter of 10 mm and thickness of 2 mm and with the disk's end surfaces always perpendicular to the axis of incident beams. The photon splitting variance reduction technique²⁹ was used with the splitting number varying from 10 to 100 depending on the radiation source quality.

II.C. Calculation of energy dependence

The energy (or beam-quality) dependence of the response of a PSD was studied by simulating the irradiation of the

TABLE I. Comparison of dose in the BC-400 scintillator attached by an air-core optical fiber with a silica tube (Fig. 2) for different particle energy cutoffs. Three orientations of the scintillator are calculated and for each orientation, the dose is normalized to that calculated with electron cutoff ECUT=512 keV and photon cutoff PCUT=1 keV. The orientation angles are defined as shown in Fig. 3.

Scintillator orientation (deg)	Relative dose in scintillator	
	ECUT=512 keV, PCUT=1 keV	ECUT=521 keV, PCUT=10 keV
0	1	$0.9975 \pm 0.17\%(1\sigma)$
90	1	$1.0025 \pm 0.14\%(1\sigma)$
180	1	$0.9995 \pm 0.17\%(1\sigma)$

detector, which is located in a water phantom with its axis perpendicular to the incident beams, by a variety of photon beams. The ratio of the dose in the sensitive region of the detector to that in the phantom without the presence of the detector (i.e., the detector dose per unit phantom dose) was then calculated. Both monoenergetic and spectrum-based photon beams were used in the calculations. The energy of the monoenergetic photon beams ranged from 150 keV to 18 MeV. All spectrum-based sources were megavoltage beams: The spectrum for the ^{60}Co beam was taken from Mora *et al.*²⁶ and the spectra for 6 and 18 MV photon beams were taken from a Monte Carlo simulation of a Varian linac.²⁷ For megavoltage beams, including spectrum-based sources and monoenergetic photon beams with energy greater than 1 MeV, the PSD was modeled at a depth of 10 cm in a cubic water phantom with 30 cm sides, with geometrical center of the detector's sensitive region at the point of measurement. The radiation source was modeled as a point source at a 100 cm source-to-surface distance with a $10 \times 10 \text{ cm}^2$ field size. For medium-energy photon beams (down to 150 keV), the PSD was modeled at a depth of 2 cm in a cubic water phantom with 20 cm sides, which corresponds to conditions of reference dosimetry for medium-energy x rays as specified by AAPM TG-61.²⁸ The radiation source was at a 20 cm source-to-surface distance with a $5 \times 5 \text{ cm}^2$ field size. These arrangements were also chosen for improving computational efficiency, as these medium-energy photons attenuate much faster in a phantom than megavoltage photons. To compare our findings to those from a previous study,²³ we also modeled a PVT scintillator embedded in a polystyrene protective layer but without the attached 3 cm optical fiber. In this case, the thickness of the polystyrene at the head of the PVT scintillator was set at 3 mm [see Fig. 1(a)]. Since there is no universal way to specify the photon beam quality for energies from 150 keV to 18 MeV, we used the photon energy or nominal energy as the quality specifier for monoenergetic photon beams or spectrum-based beams, respectively, e.g., for 6 MV linac beam, we use 6 MeV as the photon energy though the average photon energy is close to 2 MeV. For the ^{60}Co beam, we used the mean energy 1.25 MeV as the photon energy. The exact specification of beam quality is not relevant here since all high-energy data points are approximately on the same horizontal line in the graphs shown later (Figs. 4 and 5). For the realistic model of the BC-400 scintillator attached by an air-core optical fiber (Fig. 2), because of the presence of the silver layer enclosing the sensitive volume of the scintillator, we expect some impact on the response of the detector due to silver's high atomic number. Thus we also studied the variation of the energy dependence on the thickness of the silver layer either with or without the 0.16 mm silica tube. For the latter case, the silica is replaced by polystyrene in the simulation.

II.D. Calculation of angular dependence

We studied the azimuthal angular dependence of the all three PSD models for a 6 MV spectral photon beam and a 300 keV monoenergetic photon beam in a water phantom.

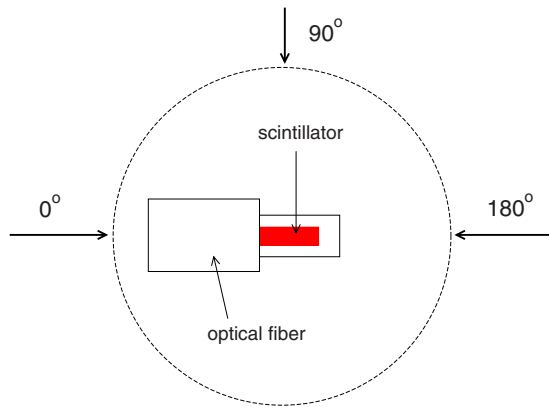


FIG. 3. Diagram showing how the azimuthal angle is defined. The thick arrows with angular degrees indicate the direction of the incident radiation beams. For example, at 90° , the radiation beam axis is perpendicular to the axis of the scintillator.

Figure 3 shows how the orientation angle of the PSD is defined relative to the incident radiation beam. The detector dose is normalized to that for the angle of 90° when the incident beam is perpendicular to the axis of the detector. For the 300 keV photon beam, since the PSD is modeled at a depth of 2 cm, the optical fiber length is set at 1.5 cm instead of 3 cm so that the entire fiber will be immersed in the phantom when the angle is 0° (i.e., when the optical fiber stem is pointing to the source). We also studied the angular dependence for a bare PVT scintillator, and a PVT scintillator with a polystyrene layer but not the optical fiber, in the 6 MV photon beam. In addition to the in-phantom simulations, we calculated the free-in-air angular dependence for the polystyrene scintillating fiber with PMMA optical fibers of different lengths. The radiation source modeled is a monoenergetic photon beam point source with an energy of 100 keV, a source-to-detector distance of 40 cm, and a field size of $5 \times 5 \text{ cm}^2$ at the detector. The space surrounding the detector and that between the source and the detector are modeled as if filled with air. The calculation results are compared to free-in-air measurements of Hyer *et al.*,⁹ which were obtained with a CT unit operating at 120 kVp.

III. RESULTS AND DISCUSSION

III.A. Energy dependence

Figure 4 shows the energy dependence of the PVT scintillator with a polystyrene protective layer but no optical fiber attached. This scintillator model is studied here solely for a comparison to a previous study by MCNP code on the same model.²³ There is no significant difference between using spectrum sources and using monoenergetic beams at megavoltage photon energies. This finding is reasonable since the curve for energy dependence of monoenergetic beams is quite flat across photon energies of almost two orders of magnitude. The results from this study agree with those from the previous study using the MCNP code, but the current statistical uncertainties are much lower ($\sim 0.5\%$). The results also agree with those obtained using the Burlin cavity

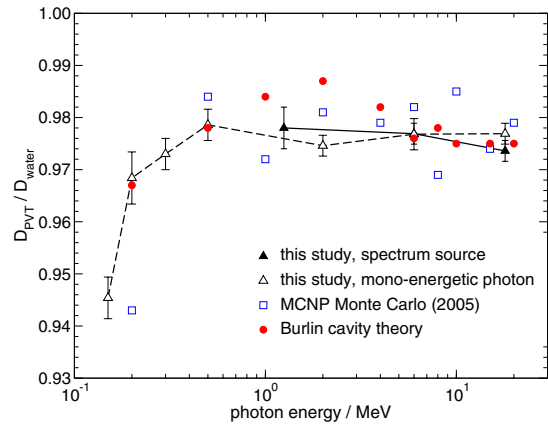


FIG. 4. The energy, or beam-quality, dependence of a BC-400 scintillator [as in Fig. 1(a) with a polystyrene thickness of 3 mm, but without attachment to the optical fiber stem]. The ordinate is the detector dose per unit phantom dose. For linac spectrum sources, the photon energy is the nominal energy of the photon beam (i.e., 6 MV is treated as 6 MeV). For the ^{60}Co beam, the mean photon energy 1.25 MeV is the photon energy. The statistical uncertainty is less than 0.5% (1σ). Solid circles are the results obtained by applying the Burlin cavity theory (Ref. 1). Open squares are the results from a previous Monte Carlo calculation with MCNP code (Ref. 23) (2%–4% 1σ uncertainty, error bar not shown). See Sec. II C for detailed geometrical information.

theory¹ except at a photon energy of 2 MeV, where the discrepancy is about 1%. This discrepancy is probably due to the limitations of the Burlin cavity theory for some of the assumptions made. The drop of the responses at lower energy end ($<300 \text{ keV}$) is due to the ratio of the mass energy absorption coefficients of water to PVT.

Figure 5 shows the energy dependence of the BC-400 scintillator coupled with the PMMA optical fiber (model 1), the BCF-12 scintillating fiber coupled with PMMA-core, glass-core, and air-core optical fibers (model 2), and the BC-

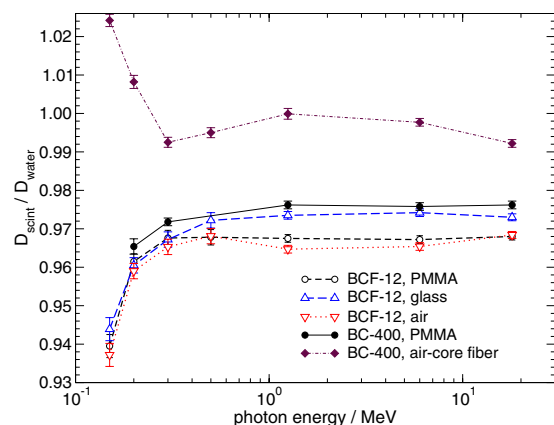


FIG. 5. The energy dependence of the BCF-12 scintillating fiber coupled with different optical fibers [Fig. 1(b)] and the BC-400 scintillator coupled with the PMMA fiber [Fig. 1(a) with a thickness of 1 mm] and the air-core fiber with a glass tube. The optical fibers are modeled as 3 cm long. The ordinate is the detector dose per unit phantom dose. For data points with photon energy greater than 1 MeV, spectrum sources are used, with the nominal energy as the abscissa. Lower energy sources ($<1 \text{ MeV}$) were monoenergetic photon beams. The statistical uncertainty is less than 0.3% (1σ).

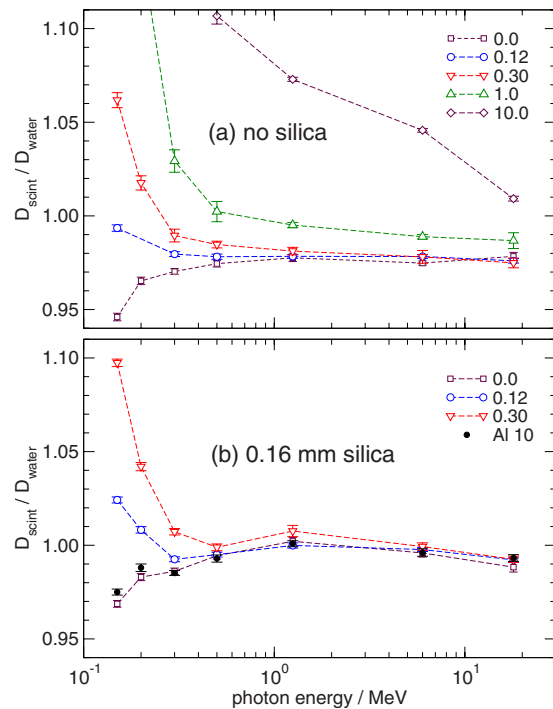


FIG. 6. The energy dependence of a BC-400 scintillator coupled with an air-core fiber with a silica (SiO_2) tube (see the model in Fig. 2) for a variety of silver thicknesses with (a) no silica present and (b) a silica thickness of 0.16 mm. The legend shows in μm the silver layer thickness except the one explicitly specified as aluminum.

400 scintillator coupled with the air-core fiber with a silica tube (model 3). Since there is no difference between using spectrum sources and using monoenergetic photon beams, the data points for both sources are combined on a single curve for each PSD. Similar to the results for the scintillator without optical fiber shown in Fig. 4, the PSDs of the models 1 and 2, made with different scintillating materials and/or different optical fiber cores, show excellent energy independence for photon energies ranging from 300 keV to 18 MV. The variations of the detector dose per unit water dose are within 0.5% at a statistical uncertainty of less than 0.2%. Below 300 keV the responses drop which is the behavior of the ratio of the mass energy absorption coefficients of water to polystyrene (or PVT). For the PSD of the third model, BC-400 with air-core fiber with silica tube, the detector dose per unit water dose is closer to unity. This is because the presence of the high-Z atoms (Si and Ag) around the sensitive volume enhances the energy deposition to the scintillator, thus making the whole response curve shifted upward by about 2%. The flatness of the detector response is a little bit worse than others but the variation is still within 1% in the photon energy range from 300 keV to 18 MV. For energies lower than 300 keV, the scintillator over-responds due to the presence of silver.

Figure 6 shows the effects of the silver layer thickness on the energy dependence of the PSD for the third model either (a) without or (b) with a 0.16 mm silica tube. In Fig. 6(a), when there is no silver layer, the curve is basically the same as that in Fig. 5 for model 1 (BC-400, PMMA). This is what

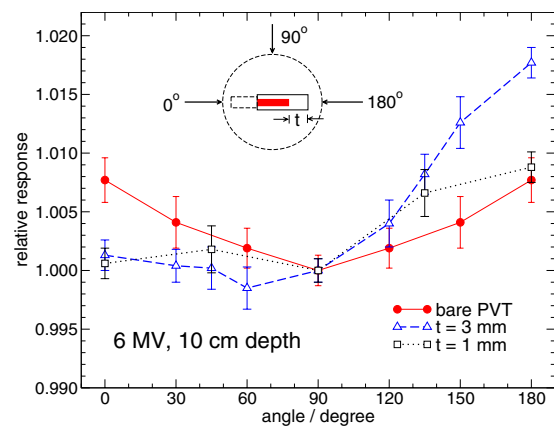


FIG. 7. The angular dependence of a bare BC-400 scintillator [as in Fig. 1(a) but without attachment to the optical fiber stem] at a depth of 10 cm in water in a 6 MV photon beam. The inset shows the definition of the angle (which is the same as in Fig. 3). In the inset, the fiber stem is drawn in dashed line indicating that it is not modeled but only for identification purpose. The detector dose at any angle is normalized to that at 90° . Two tip thicknesses $t=1$ mm and $t=3$ mm are studied. The statistical uncertainty is less than 0.3% (1σ).

we expected since the polystyrene is close to water equivalent. A silver layer of $1 \mu\text{m}$ will have a significant effect on the detector: Increasing the response by a couple of percent in megavoltage region and dramatically for photon energies below 300 keV. A silver layer thickness of $10 \mu\text{m}$ will make the detector essentially useless because of the very large energy dependence. For the silver layer thickness of $0.3 \mu\text{m}$ or less, it has negligible effects on the response for megavoltage photon beams but still has significant effect for photon energies less than 300 keV. In Fig. 6(b), due to the presence of the 0.16 mm silica tube, all the curves (for silver thickness $\leq 0.3 \mu\text{m}$) are shifted upward by about 2%–3%. Figure 6 demonstrates that even for a small variation of thickness ($\sim 0.3 \mu\text{m}$) of the silver layer, there is a more than 5% change on the response of the detector for photon energy of 200 keV. As the purpose of the silver coating is to prevent the optical light exchange at the silica and the scintillator/air boundary, one way to minimize the variation of the detector response at lower photon energy is to use aluminum coating instead of silver. Figure 6(b) also shows the result for a $10 \mu\text{m}$ aluminum coating, which is almost the same as the result for zero thickness silver layer because the atomic number of aluminum is only one less than silicon and $10 \mu\text{m}$ is negligible compared to the 0.16 mm silica.

III.B. Angular dependence

Figure 7 shows the angular dependence of the bare PVT scintillator simulated at a 10 cm depth in a water phantom irradiated by a 6 MV photon beam. The figure also shows the azimuthal angle between the detector and the incident beam. The detector dose at any azimuthal angle is normalized to that calculated at 90° . For the bare scintillator, because of the symmetry, only responses for angles from 90° to 180° are calculated. The relative response varies at most 0.8%. When the polystyrene tip thickness is 1 mm, the angular variation

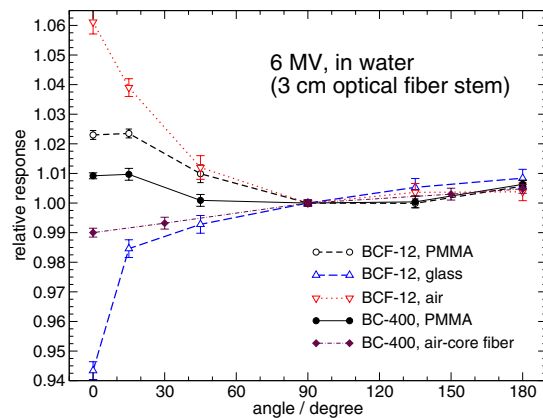


FIG. 8. The angular dependence of the BCF-12 scintillating fiber coupled with different optical fibers [Fig. 1(b)] and the BC-400 plastic scintillator coupled with the PMMA fiber [Fig. 1(a) with thickness at the tip of 1 mm] and the air-core fiber with a glass tube at a 10 cm depth in a water phantom in a 6 MV photon beam. Angles are defined as shown in Fig. 3. The detector dose at any angle is normalized to that at 90°. The length of the optical fibers is modeled as 3 cm. The statistical uncertainty is less than 0.3% (1σ).

of the response is about the same as that of the bare scintillator. For a 3 mm polystyrene tip thickness, the angular variation of the response could be as large as 1.8%. These results suggest that minimizing the thickness of the protective layer at the head of a PSD may reduce the angular dependence of the detector's response. Figure 8 shows the angular dependence of the three PSD models simulated at a 10 cm depth in a water phantom in the 6 MV photon beam. For simulations in which the detector head points toward the radiation source (i.e., angles greater than 90°), the response of the PSDs for all three models remains almost constant (within 1%), regardless of the optical fiber core material. When the detector head points away from the radiation source (i.e., angles less than 90°), conversely, the response of the PSDs varies depending on the optical fiber material. At 0°, with the stem pointing directly to the source, the detector's response could be 6% higher than at 90° when it is attached to an air-core fiber (BCF-12, model 2) and 6% lower when it is attached to a glass-core fiber. (Note, however, that these values are for a fiber stem length of 3 cm.) This is mainly an attenuation issue: Air causes less attenuation on the incident photon beam than water, but glass (SiO_2) causes more attenuation than water due to its higher density and effective atomic number. However, for the PMMA-core optical fiber, the effect is at most 2% for all angles for its close to water equivalent. For the BC-400 scintillator coupled with the air-core fiber with a silica tube (model 3), the variation of the response for all angles is also within 2%. This behaves differently from the other PSD with air-core fiber in model 2 because the presence of high-Z atoms (Si and Ag) in the air-core fiber in model 3 happens to compensate the effect of air.

Figure 9 shows the angular dependence for all of these PSD models in a water phantom irradiated by a 300 keV monoenergetic photon beam. The relative response of the detectors deviates significantly from unity only for angles

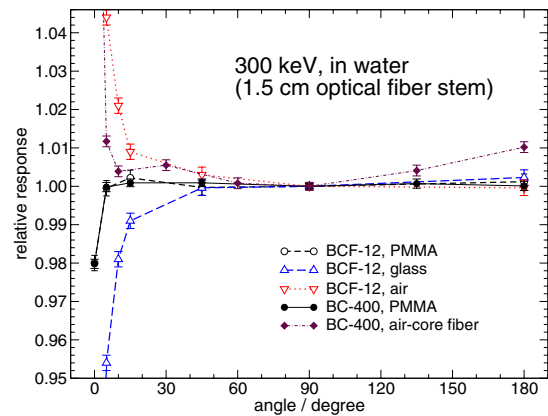


FIG. 9. The angular dependence of the BCF-12 scintillating fiber coupled with different optical fibers [Fig. 1(b)] and the BC-400 plastic scintillator coupled with the PMMA fiber [Fig. 1(a) with a tip thickness of 1 mm] and the air-core fiber with a glass tube at a 2 cm depth in a water phantom in a 300 keV monoenergetic photon beam. The angle is defined as shown in Fig. 3. The detector dose at any angle is normalized to that at 90°. The length of the optical fibers is modeled as 1.5 cm. The relative responses for the scintillating fiber attached to optical fibers with glass and air cores at 0° are 0.83 and 1.15, respectively. The statistical uncertainty is less than 0.3% (1σ).

very close to 0°. For angles greater than 10°, the relative response of all the detectors varies within 2% regardless of the models or the optical fiber core material used. This result is true even at 0° for the detectors attached by the PMMA-core optical fiber. For the PSD attached to an air-core optical fiber (BCF-12, model 2), the detector's response at 0° could be about 15% higher than at 90°, and for the glass-core fiber it is about 15% lower. The apparent different behaviors of the angular dependence between Figs. 8 and 9 can be explained by the fact that the phantom scattering for the 6 MV photon beam is much higher than that for the 300 keV beam, and the effect of attenuation by the fiber stem, i.e., photoelectric absorption, is much larger in 300 keV beam than in 6 MV beam. For example, for the BC-400 PSD with air-core fiber (model 3) at 0°, the effects of air and high-Z atoms (Si and Ag) compensate mutually in the 6 MV beam where Compton effect dominates; they no longer cancel each other in the 300 keV beam where photoelectric effect becomes important.

Figure 10 shows the free-in-air calculations of the angular dependence of the BCF-12 scintillating fiber coupled to a PMMA-core fiber stem 3 or 10 cm long in a 100 keV monoenergetic photon beam. There is essentially no scatter in this case, so the drop in signal at 0° is very steep compared to that in the phantom case (Fig. 9). The length of the optical fiber stem mainly has an effect at 0° due to attenuation by the fiber. The calculated angular dependence agrees qualitatively with the measurements as far as the large drop in response near 0° is concerned. Quantitatively, however, there is still disagreement between the calculations and the experiments since we were not able to model the exact material and geometrical data used in the experiments. The factors most responsible for the disagreement would be the length and path of the curved fiber exposed to the radiation and the material and shape of the detector holder. Using a monoenergetic x-ray beam instead of a more realistic spectrum source might

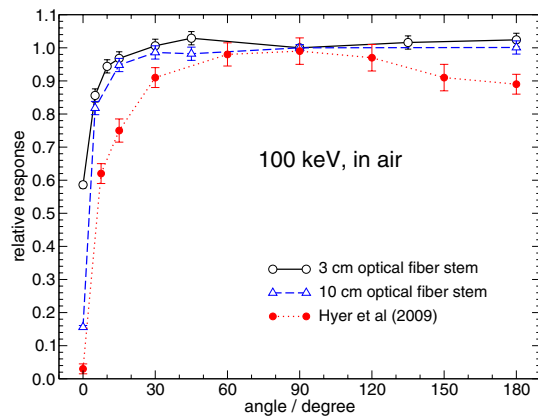


FIG. 10. The angular dependence of the BCF-12 scintillating fiber coupled with PMMA plastic optical fibers with lengths of 3 and 10 cm irradiated free-in-air by a 100 keV monoenergetic photon beam. The angle is defined here as shown in Fig. 3. The detector dose at any angle is normalized to that at 90°. The statistical uncertainty for the calculation is around 2% (1σ). The solid symbols represent a measurement by Hyer *et al.* (Ref. 9), who used a clinical CT unit operating at 120 kVp. Because of the detectors' symmetry, only half the data (0°–180°) are taken from Fig. 8 in their paper.

also result in some differences. Another factor to be noted is that the measured data are normalized at 90° where the data point itself has an uncertainty of about 5%. So, for example, if the response at this angle happens to be overestimated by 5%, then the actual measured curve would be shifted upward by 5%, which would make the agreement better.

IV. CONCLUSIONS

In this study, we used Monte Carlo simulations to investigate the response of PSDs to photon beams. A plastic scintillator (BC-400) and a scintillating fiber (BCF-12), both attached by a plastic-core optical fiber stem, are modeled. Also studied is a plastic scintillator (BC-400) attached by an air-core optical fiber stem with a silica tube coated with silver. The detectors' responses are calculated as the detector dose per unit phantom dose. For the energy dependence of the PSDs in photon beams, the calculations show that the PSDs with plastic-core fiber have excellent energy independence within about 0.5% with a low ($<0.3\%$, 1σ) statistical uncertainty at photon energies ranging from 300 keV (monoenergetic) to 18 MV (linac beam). The PSD with an air-core optical fiber with a silica tube also has good energy independence within 1% in the same photon energy range and it is even closer to water equivalent due to the presence of silica wall around the scintillator. About the angular dependence, the relative response of all the three modeled PSDs is within 2% for all the angles in a 6 MV photon beam. This is also true in a 300 keV monoenergetic photon beam for PSDs with plastic-core fiber. For the PSD with an air-core fiber with a silica tube in the 300 keV beam, the relative response varies within 1% for most of the angles except in the case when the fiber stem is pointing right to the radiation source in which case the PSD may over-respond by more than 10%. For a PSD with a glass-core fiber in either photon beams, the variation of the response is also within 2% for most of the

angles except when the fiber stem is pointing to the radiation source. These results suggest that for most situations where the orientation of the detectors can be controlled, the angular dependence of PSDs is not of concern no matter what kind of material is used for the optical fiber core. For *in vivo* applications, especially for intensity-modulated radiation therapy or arc therapy, since the detector's orientation cannot be guaranteed once it has been inserted into the patient's body and since the radiation beam may come from various directions, it is probable that the optical fiber stem could point directly to the source. In this extreme condition, the response of PSDs either with plastic-core fiber or with air-core fiber with a silica tube has a maximum deviation of 2%, while a PSD with glass-core fiber would have large deviations in dose reading thus should be avoided.

ACKNOWLEDGMENTS

The authors are very thankful to the associate editor and an anonymous referee for their comments which have helped to improve this manuscript a lot. This research was supported by the National Cancer Institute (NCI) Grant No. 1R01CA120198-01A2 and NIH/NCI Grant No. T32 CA119930-04.

^{a)} Author to whom correspondence should be addressed. Electronic mail: abeddar@mdanderson.org; Telephone: (713) 563-2609; Fax: (713) 563-2479.

¹ A. S. Beddar, T. R. Mackie, and F. H. Attix, "Water-equivalent plastic scintillation detectors for high-energy beam dosimetry: I. Physical characteristics and theoretical considerations," *Phys. Med. Biol.* **37**, 1883–1900 (1992).

² A. S. Beddar, T. R. Mackie, and F. H. Attix, "Water-equivalent plastic scintillation detectors for high-energy beam dosimetry: II. Properties and measurements," *Phys. Med. Biol.* **37**, 1901–1913 (1992).

³ D. Flühs, M. Heintz, F. Indenkamp, C. Wieczorek, H. Kolanoski, and U. Quast, "Direct reading measurement of absorbed dose with plastic scintillators—The general concept and applications to ophthalmic plaque dosimetry," *Med. Phys.* **23**, 427–434 (1996).

⁴ L. Archambault, A. S. Beddar, L. Gingras, R. Roy, and L. Beaulieu, "Measurement accuracy and Čerenkov removal for high performance, high spatial resolution scintillation dosimetry," *Med. Phys.* **33**, 128–135 (2006).

⁵ J. Lambert, D. R. McKenzie, S. Law, J. Elsey, and N. Suchowerska, "A plastic scintillation dosimeter for high dose rate brachytherapy," *Phys. Med. Biol.* **51**, 5505–5516 (2006).

⁶ A. R. Beierholm, C. E. Andersen, L. R. Lindvold, F. Kjaer-Kristoffersen, and J. Medin, "A comparison of BCF-12 organic scintillators and $\text{Al}_2\text{O}_3\text{:C}$ crystals for real-time medical dosimetry," *Radiat. Meas.* **43**, 898–903 (2008).

⁷ M. Eichmann, D. Flühs, and B. Spaan, "Development of a high precision dosimetry system for the measurement of surface dose rate distribution for eye applicators," *Med. Phys.* **36**, 4634–4643 (2009).

⁸ L. Archambault, J. C. Polf, L. Beaulieu, and S. Beddar, "Characterizing the response of miniature scintillation detectors when irradiated with proton beams," *Phys. Med. Biol.* **53**, 1865–1876 (2008).

⁹ D. E. Hyer, R. F. Fisher, and D. E. Hintenlang, "Characterization of a water equivalent fiber-optic coupled dosimeter for use in diagnostic radiology," *Med. Phys.* **36**, 1711–1716 (2009).

¹⁰ L. E. Cartwright, J. Lambert, D. R. McKenzie, and N. Suchowerska, "The angular dependence and effective point of measurement of a cylindrical scintillation dosimeter with and without a radio-opaque marker for brachytherapy," *Phys. Med. Biol.* **54**, 2217–2227 (2009).

¹¹ I. Kawrakow and D. W. O. Rogers, "The EGSnrc code system: Monte Carlo simulation of electron and photon transport," Technical Report No. PIRS-701 (National Research Council of Canada, Ottawa, Canada, 2000). See also <http://www.irs.inms.nrc.ca/inms/irs/EGSnrc/EGSnrc.html>.

- ¹²I. Kawrakow, "Accurate condensed history Monte Carlo simulation of electron transport. I. EGSnrc, the new EGS4 version," *Med. Phys.* **27**, 485–498 (2000).
- ¹³E. Brannen and G. L. Olde, "The response of organic scintillators to electron energy deposited in them," *Radiat. Res.* **16**, 1–6 (1962).
- ¹⁴D. L. Smith, R. G. Polk, and T. G. Miller, "Measurement of the response scintillators to electrons, protons and deuterons," *Nucl. Instrum. Methods* **64**, 157–166 (1968).
- ¹⁵A. S. Beddar, S. Law, N. Suchowerska, and T. R. Mackie, "Plastic scintillation dosimetry: Optimization of light collection efficiency," *Phys. Med. Biol.* **48**, 1141–1152 (2003).
- ¹⁶A. S. Beddar, N. Suchowerska, and S. H. Law, "Plastic scintillation dosimetry for radiation therapy: Minimizing capture of Cerenkov radiation noise," *Phys. Med. Biol.* **49**, 783–790 (2004).
- ¹⁷A. S. Beddar, T. R. Mackie, and F. H. Attix, "Cerenkov light generated in optical fibres and other light pipes irradiated by electron beams," *Phys. Med. Biol.* **37**, 925–935 (1992).
- ¹⁸S. F. de Boer, A. S. Beddar, and J. A. Rawlinson, "Optical filtering and spectral measurements of radiation-induced light in plastic scintillation dosimetry," *Phys. Med. Biol.* **38**, 945–958 (1993).
- ¹⁹M. A. Clift, P. N. Johnston, and D. V. Webb, "A temporal method of avoiding the Cerenkov radiation generated in organic scintillator dosimeters by pulsed mega-voltage electron and photon beams," *Phys. Med. Biol.* **47**, 1421–1433 (2002).
- ²⁰A.-M. Frelin, J.-M. Fontbonne, G. Ban, J. Colin, M. Labalme, A. Batalla, A. Isambert, A. Vela, and T. Leroux, "Spectral discrimination of Cerenkov radiation in scintillating dosimeters," *Med. Phys.* **32**, 3000–3006 (2005).
- ²¹J. Lambert, Y. Yin, D. R. McKenzie, S. Law, and N. Suchowerska, "Cerenkov-free scintillation dosimetry in external beam radiotherapy with an air core light guide," *Phys. Med. Biol.* **53**, 3071–3080 (2008).
- ²²P. Naseri, N. Suchowerska, and D. R. McKenzie, "Scintillation dosimeter arrays using air core light guides: Simulation and experiment," *Phys. Med. Biol.* **55**, 3401–3415 (2010).
- ²³A. S. Beddar, T. M. Briere, F. A. Mourtada, O. N. Vassiliev, H. H. Liu, and R. Mohan, "Monte Carlo calculations of the absorbed dose and energy dependence of plastic scintillators," *Med. Phys.* **32**, 1265–1269 (2005).
- ²⁴LANL, "MCNPX user's manual version 2.4.0," Los Alamos National Laboratory Report No. LA-UR-02–5253, edited by L. S. Waters, 2002.
- ²⁵D. Létourneau, J. Pouliot, and R. Roy, "Miniature scintillating detector for small field radiation therapy," *Med. Phys.* **26**, 2555–2561 (1999).
- ²⁶G. Mora, A. Maio, and D. W. O. Rogers, "Monte Carlo simulation of a typical ⁶⁰Co therapy source," *Med. Phys.* **26**, 2494–2502 (1999).
- ²⁷D. Sheikh-Bagheri and D. W. O. Rogers, "Monte Carlo calculation of nine megavoltage photon beam spectra using the BEAM code," *Med. Phys.* **29**, 391–402 (2002).
- ²⁸C.-M. Ma, C. W. Coffey, L. A. DeWerd, R. Nath, C. Liu, S. M. Seltzer, and J. Seuntjens, "AAPM protocol for 40–300 kV x-ray beam dosimetry in radiotherapy and radiobiology," *Med. Phys.* **28**, 868–893 (2001).
- ²⁹I. Kawrakow, "EGSnrc C++ class library," NRC Technical Report No. PIRS-898 (National Research Council of Canada, Ottawa, Canada, 2005). See also <http://www.irs.inms.nrc.ca/EGSnrc/pirs898/>.

Plastic scintillation dosimetry: Optimal selection of scintillating fibers and scintillators

Louis Archambault, Jean Arsenault, Luc Gingras, A. Sam Beddar, René Roy, and Luc Beaulieu

Citation: *Medical Physics* **32**, 2271 (2005); doi: 10.1118/1.1943807

View online: <http://dx.doi.org/10.1118/1.1943807>

View Table of Contents: <http://scitation.aip.org/content/aapm/journal/medphys/32/7?ver=pdfcov>

Published by the [American Association of Physicists in Medicine](#)

Articles you may be interested in

[Monte Carlo study of the energy and angular dependence of the response of plastic scintillation detectors in photon beams](#)

Med. Phys. **37**, 5279 (2010); 10.1118/1.3488904

[Simulation of the precision limits of plastic scintillation detectors using optimal component selection](#)

Med. Phys. **37**, 412 (2010); 10.1118/1.3276734

[Exploration of the potential of liquid scintillators for real-time 3D dosimetry of intensity modulated proton beams](#)

Med. Phys. **36**, 1736 (2009); 10.1118/1.3117583


[Experience-driven dose-volume histogram maps of NTCP risk as an aid for radiation treatment plan selection and optimization](#)

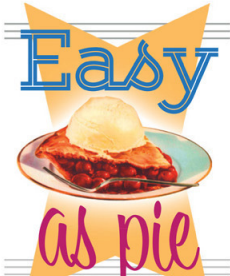
Med. Phys. **35**, 333 (2008); 10.1118/1.2815943

[Development and characterization of a tissue equivalent plastic scintillator based dosimetry system](#)

Med. Phys. **33**, 96 (2006); 10.1118/1.2140118

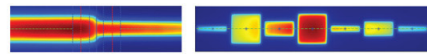
Read the full article online for free at





RITG148⁺


Custom Designed
TG-148 Tests
For Tomotherapy QA



RIT is your only source for the tests specified for helical tomotherapy in the TG-148 report. These automated QA tests include:

<ul style="list-style-type: none"> Automated QA testing Y-jaw divergence/beam centering Y-jaw/gantry rotation plane alignment Gantry angle consistency Treatment field centering 	<ul style="list-style-type: none"> MLC alignment test Couch translation/gantry rotation Laser localization Image quality tests (Cheese Phantom) Built in trending and reporting with RITrend
---	---

These tests are included in both our RITComplete, and RITG148+ products.



Call 719.590.1077,
option 4, or email
mac@radimage.com
today to set up your
personal demo.

Plastic scintillation dosimetry: Optimal selection of scintillating fibers and scintillators

Louis Archambault,^{a)} Jean Arsenault, and Luc Gingras

*Département de Radio-Oncologie et Centre de Recherche en Cancérologie, Hôtel-Dieu de Québec,
11 côte du palais, Québec, Québec G1R 2J6, Canada, and Département de Physique,
de Génie Physique et d'Optique, Université Laval, Québec, Québec Canada*

A. Sam Beddar

*Department of Radiation Physics, The University of Texas M. D. Anderson Cancer Center,
Houston, Texas 77030*

René Roy

Département de Physique, de Génie Physique et d'Optique, Université Laval, Québec, Québec, Canada

Luc Beaulieu

*Département de Radio-Oncologie et Centre de Recherche en Cancérologie, Hôtel-Dieu de Québec,
11 côte du palais, Québec, Québec G1R 2J6, Canada and Département de Physique,
de Génie Physique et d'Optique, Université Laval, Québec, Québec, Canada*

(Received 22 December 2004; revised 26 April 2005; accepted for publication 1 May 2005;
published 20 June 2005)

Scintillation dosimetry is a promising avenue for evaluating dose patterns delivered by intensity-modulated radiation therapy plans or for the small fields involved in stereotactic radiosurgery. However, the increase in signal has been the goal for many authors. In this paper, a comparison is made between plastic scintillating fibers and plastic scintillator. The collection of scintillation light was measured experimentally for four commercial models of scintillating fibers (BCF-12, BCF-60, SCSF-78, SCSF-3HF) and two models of plastic scintillators (BC-400, BC-408). The emission spectra of all six scintillators were obtained by using an optical spectrum analyzer and they were compared with theoretical behavior. For scintillation in the blue region, the signal intensity of a singly clad scintillating fiber (BCF-12) was 120% of that of the plastic scintillator (BC-400). For the multiclاد fiber (SCSF-78), the signal reached 144% of that of the plastic scintillator. The intensity of the green scintillating fibers was lower than that of the plastic scintillator: 47% for the singly clad fiber (BCF-60) and 77% for the multiclاد fiber (SCSF-3HF). The collected light was studied as a function of the scintillator length and radius for a cylindrical probe. We found that symmetric detectors with nearly the same spatial resolution in each direction (2 mm in diameter by 3 mm in length) could be made with a signal equivalent to those of the more commonly used asymmetric scintillators. With augmentation of the signal-to-noise ratio in consideration, this paper presents a series of comparisons that should provide insight into selection of a scintillator type and volume for development of a medical dosimeter. © 2005 American Association of Physicists in Medicine. [DOI: 10.1118/1.1943807]

Key words: plastic scintillator, scintillating fibers, dosimetry, optical fibers, Cerenkov light, small fields

I. INTRODUCTION

Radiotherapy dosimetry requires detectors with an excellent level of precision in dose measurement, since the treatment outcome is highly dependent on the accuracy of radiation delivery.¹ With its well-known response, the ionization chamber has been the reference standard for dosimetry measurements and the benchmark for this kind of application for decades. However, complex irradiation schemes with the small fields that occur in intensity-modulated radiation therapy (IMRT) and stereotactic radiosurgery, present a large number of high-dose gradients within a given field, thus requiring high spatial resolution in the measurement. Dose discrepancies as high as 10% have been reported with standard-size ionization chambers between the cross-profile of an intensity-modulated beam and the planned values.² This can

be explained by the averaging effect of the detectors due to their relatively large detecting volumes.^{3,4} Although small volume chambers can be used, their output signal is significantly smaller, and their sensitivity is lower owing to a reduction in ionization deposition. Solid-state detectors could potentially solve this problem, but they are highly nonwater-equivalent and have other drawbacks such as dose rate and energy dependence for diodes and a limited lifetime for MOSFETs. Scintillation dosimeters are therefore an interesting avenue to solution of many of these issues.

A. A brief overview of scintillation detectors

A scintillation dosimeter system comprises three main components: a detector probe, a light guide, and a photode-

tector. The detector probe, or sensitive volume, is most frequently composed of a small volume plastic scintillator,^{5,6} but detectors with scintillating fibers⁷ or scintillator sheets⁸ have also been reported. The second component of the system is the light guide, generally made from optical fibers, which transports the light produced in the detector probe to the photodetector. The third component converts the scintillation light into a readable signal. This task can be performed by devices such as photomultiplier tubes⁵ or photodiodes.⁶ In a detailed study of small volume scintillators (1 mm in diameter by 4 mm in length) used for high-energy beam dosimetry, Beddar *et al.* and Clift *et al.* experimentally tested dose and dose rate linearity, spatial resolution, temperature dependence, and radiation resistance.^{5,9–11} These authors showed that these properties make scintillation dosimeters well adapted to most radiotherapy applications. However, when exposed to electron beams, these detectors may be subject to strong stem effect resulting from Cerenkov radiation in the optical components of the detector, which has a negative effect on the signal-to-noise ratio (SNR).

Plastic scintillators possess advantageous dosimetric characteristics: an intrinsic water equivalence of the plastic materials (PMMA [polymethylmethacrylate] and polystyrene in the case of scintillating fibers and polyvinyltoluene in the case of plastic scintillators) and linear response to dose, dose rate, and energy down to 125 keV.¹ Those properties make plastic scintillators a valuable dosimetric tool for the quality assurance of complex treatment plans. Furthermore, these detectors have been shown to be capable of accurately determining the absorbed dose and the dose distribution in a comparative study of small volume dosimeters (semiconductor diode, liquid chamber, and diamond detector) in narrow high-energy photon beam dosimetry.¹²

B. The Cerenkov effect

Cerenkov radiation occurs when a particle's velocity exceeds the speed of light in a given medium.¹³ The number of photons N_{crkv} produced by this effect for a given wavelength λ decreases as $1/\lambda^3$. Over the entire visible spectrum, N_{crkv} is low, but in scintillation dosimeters, a large part of the light guide can be in the radiation field with the consequence that Cerenkov radiation may become a significant source of stem effect, especially in the case of electron irradiation. It is important to state that even if there is some Cerenkov radiation produced inside the scintillator probe, the large majority is produced in the optical fiber so that the probe itself has no impact on the total Cerenkov component of the signal.

Cerenkov radiation is not suitable for dosimetric purposes because even if N_{crkv} depends on the radiation dose received by the optical fiber, it also depends on the length of optical fiber in the radiation field as well as its angle with respect to the incident radiation, both of which can vary for each measurement. When the length of optical fiber in the field and the angle of incident radiation is more or less constant between measurements, the Cerenkov light can be proportional to the

dose delivered. In this case, the stem effect reduces the spatial resolution of the detector and still needs to be removed from the scintillation signal.

Several published studies deal with methods to minimize the stem effect caused by Cerenkov radiation with different levels of complexity and accessibility. One of the first techniques used was the background subtraction technique, in which the signal from an optical fiber unattached to the scintillator, detecting only background radiation, was subtracted from the signal from the fiber attached to the scintillator.^{5,6} However, to be valid, this technique requires that both fibers receive the same dose gradient, which may not be the case for the high dose gradients encountered in IMRT. Because most of the emission spectrum for Cerenkov light occurs in the lower blue region of the visible spectrum, attempts were made by Boer *et al.*¹⁴ and later by Clift *et al.*¹⁵ to remove the bluest component of light reaching the photodetector. To do this, the authors used long pass filters and scintillators designed to emit at longer wavelengths. However, orange scintillators are generally less efficient than blue ones and filters attenuate the signal along with the noise. Thus even if an increase in the SNR was observed, the total signal would not be sufficient to preclude use of the background subtraction technique. Another noise reduction technique is temporal gating of the signal by using the pulsed beams of a linear accelerator and a scintillating material with a decay constant larger than that of the Cerenkov light. Most of those systems were developed with an inorganic (i.e., nonwater-equivalent) scintillator.^{16,17} One of the first inorganic scintillator dosimeters used in radiotherapy was developed by Jordan.¹⁶ In this particular case, a spherical ruby detector (1 mm in diameter) was used with an emission lifetime around 3 ms. With this system, it was possible to accurately measure dose in electron fields (4 and 12 MeV), since the main source of noise was statistical variation instead of the Cerenkov stem effect. A time-gated prototype of a plastic scintillator was recently tested under an electron beam and was found to be inadequate because of loss of most of the scintillation signal after the gating.¹⁸ Scintillators with larger volumes (1 cm in diameter by 2 cm in length) have also been used with success for daily quality assurance,^{19,20} but these detectors do not possess the high spatial resolution required for IMRT and stereotactic radiosurgery. Some encouraging results have been obtained by using the signal from two color bands (blue and green) to extract the scintillation from the noisy output.⁷ This technique requires only an initial calibration and does not need a background fiber.

With increase of the scintillation signal relative to the Cerenkov stem effect in mind, we present a careful examination of commercially available scintillators and scintillating fibers. This is complementary to the above-mentioned techniques, and should provide insight into the selection of a scintillator type and volume for development of an improved plastic scintillation detector ideal for IMRT and stereotactic radiosurgery verifications.

TABLE I. Fiber models and dimensions.

Name	Type (# clad)	Diameter (mm)	λ_{peak} (nm)
SCSF-3HF(1500)	Fiber (2)	1	530
SCSF-78	Fiber (2)	1	450
BCF-60	Fiber (1)	1	530
BCF-60	Fiber (1)	2	530
BCF-60	Fiber (1)	3	530
BCF-12	Fiber (1)	1	435
BC-400	Scintillator	1	423
BC-408	Scintillator	1	425

II. METHODS AND MATERIALS

A. Scintillator detector materials

Water equivalence of plastic scintillators is a great advantage for dosimetric purposes,^{5,6} and having a detector with a submillimeter radius would significantly improve the accuracy of measurements in regions with high dose gradients, such as those that occur in IMRT and stereotactic radiosurgery. Increasing the signal of scintillator-based detectors without increasing their size would make them more robust by reducing statistical variation between measurements. It would also make them more versatile by allowing them to be used in electron fields, or in regions of small dose and/or large dose gradients.

In this study, two types of scintillator are tested: the plastic scintillator and the plastic scintillating fiber, both of which were cylindrical in shape. Their spectra and total emission intensities were compared to those of plastic scintillators (see Sec. II B). Inorganic scintillating fiber also exists, but has not been considered in this work.

1. Plastic scintillators

The two commercial plastic scintillators used [Saint-Gobain Crystals and Detectors, Paris, France] are made of Polyvinyltoluene which has a density of 1.032 g/cc. Their properties are listed in Table I.

A photon produced in a plastic scintillator of index n_{sci} is transmitted along the optical fiber only if its angle with respect to the optical fiber axis is less than a given acceptance angle a :

$$a = \sin^{-1} \left(\frac{1}{n_{\text{sci}}} \sqrt{n_{\text{co}}^2 - n_{\text{cl}}^2} \right), \quad (1)$$

where n_{co} and n_{cl} are the refractive indices of optical fiber core and cladding, respectively.

As stated by Beddar *et al.*, the acceptance efficiency ε_a of an optical fiber is defined as the amount of scintillation light that can be coupled to the optical fiber.²¹ If the scintillation emission can be considered isotropic, then ε_a can be defined as the fraction of solid angle described by a cone of half angle a :²¹

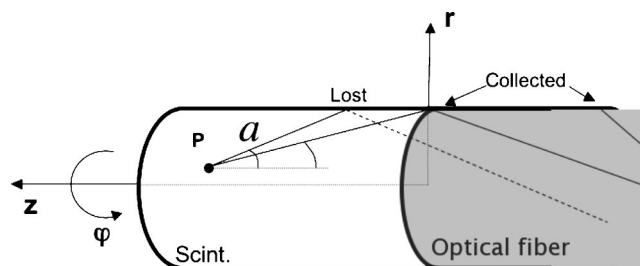


FIG. 1. Schematic of a plastic scintillator.

$$\varepsilon_a = \frac{1}{4\pi} \int d\Omega. \quad (2)$$

Collection is restricted by the difference of index between n_{sci} and n_{co} , but in practice it is maximized by the use of index matching liquid. Other restrictions come from the attenuation inside a plastic scintillator and its finite volume. The total radiation dose will also reduce the attenuation length,²² but this process is relatively slow. The finite volume may limit collection efficiency, since there are positions for which a photon produced at an angle a will hit the wall of the detector before it reaches the collecting fiber. An example is given in Fig. 1. At the scintillator-air interface, the photon will either be reflected or be transmitted, it depends on several factors discussed in the next section.

2. Plastic scintillating fibers

At first, a plastic-air interface can appear as the optimal choice for light collection inside the scintillator since this combination possesses the highest critical angle. However, because the angle with the scintillator wall at every internal reflection is constant (by Snell's law), photons reflected at angles higher than a reaching the optical fiber will not be accepted. Therefore, a higher collection inside the scintillator will not always result in an increased light collection by the optical fiber. Moreover, to take full advantage of the collection efficiency caused by total reflexion in a plastic scintillator, its surface has to be carefully polished and its surrounding should be of a smaller refraction index.

Plastic scintillating fibers²³ (see Fig. 2) have been considered an alternative to plastic scintillators because the addition of a nonscintillating cladding over a scintillating core makes this kind of scintillator less dependent on the surface polishing, surface damage, and the general surrounding of

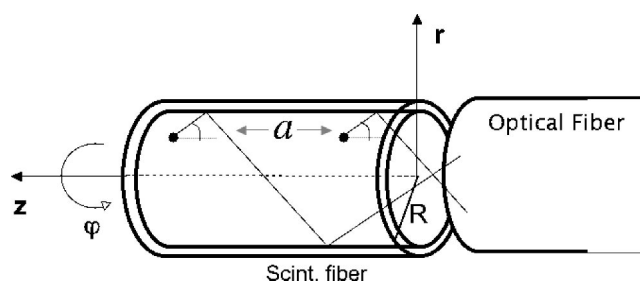


FIG. 2. Schematic of a scintillating fiber.

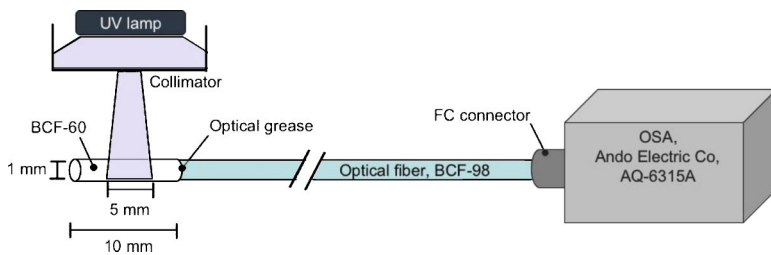


FIG. 3. Schematic illustration of the experiments using an optical spectrum analyzer (OSA).

the detector. Moreover, the manufacturers of scintillating fiber use a cladding relatively thick in order to increase the robustness to physical damages. For the fibers used in this study, cladding represents 3% of the nominal diameter, meaning that its sensitive volume is 12% smaller than that of a plastic scintillator with the same diameter. The scintillating fibers used in this work (BCF [Saint-Gobain Crystals and Detectors, Paris, France] and SCSF [Kuraray co. Tokyo, Japan], see Table I for more details) have a core made of polystyren (density of 1.05 g/cc) and a cladding made of acrylic. The reason why commercial scintillating fibers are made of a different material than plastic scintillator is for their longer attenuation length since numerous applications outside radiotherapy use long segments of scintillating fiber.

The refractive index difference between the core and cladding of the plastic scintillating fibers is sufficient to generate a critical angle larger than the acceptance angle of most optical fibers. Therefore if the attenuation inside the the scintillating fiber is neglected, the collection efficiency for every point inside the dosimeter is given by the integration of Eq. (2):

$$\varepsilon_a = \frac{1}{2}(1 - \cos(a)). \quad (3)$$

B. Experimental measurements

The spectrum and total light emission of each scintillator were evaluated for diameters between 0.5 and 3 mm and lengths between 3 and 12 mm. Light emission measurements were performed by using either ultraviolet stimulation and an optical spectrum analyzer (OSA, AQ6315 A; Ando Electric Co., Kanagawa, Japan) measurement (see Sec. III A) or ^{60}Co irradiation and a photodiode measurement (see Secs. III B and III C). Each measurement is described in detail in the following sections.

1. Spectral measurement apparatus

The emission spectra of the various scintillating materials were experimentally measured using an OSA. Since the light yield under megavoltage radiation of scintillating fibers and scintillators was not intense enough to accumulate a signal with an OSA, it was necessary to stimulate light emission with an ultraviolet lamp that generate UVA radiation (315–380 nm). A collimator was built to send a light field with dimensions of $5 \times 2 \text{ mm}^2$ on plastic scintillators or scintillating fibers, with the largest side of the field aligned along the long axis of the scintillating fiber. The scintillating samples used were cut to lengths of 10 mm and coupled to optical

fibers using optical grease inside an acrylic sleeve with a hole diameter of 1 mm to keep the bond in place. A 20 cm section of optical fiber with the same radius was used to carry the light to the OSA. Both ends of this light guide were prepared in the same manner as the scintillating fibers. One of its extremities was glued to an FC connector and fixed to the OSA (see Fig. 3).

2. Scintillation light measurements

To verify the impact of scintillator length, a scintillating fiber (BCF-60) and a plastic scintillator (BC-408) were placed under a clinical beam of cobalt-60 radiation. The produced light was coupled to an optical fiber (1 mm diameter, BCF-98) as in the previous section and sent to a photodiode. The photodiode noise and Cerenkov light were removed by subtracting the signal produced by an optical fiber irradiated in the exact same conditions but with no scintillator attached to it. After each irradiation, a small piece of the scintillating material was cut.

The impact of the scintillating fiber diameter on light emission was tested in two different ways for the three different sizes of the BCF-60 scintillating fiber available: 1, 2, and 3 mm. Measurements were first made to verify that the total light was produced proportionally to the total volume of the scintillating fiber. A first set of measurements were done by directly placing a 50 mm length of scintillating fiber in contact with a photomultiplier tube (PMT) and irradiating the last 15 mm for a given time. For these irradiations, a small cobalt-60 source was used with an activity less than 20 μCi , and 200-mm-thick lead shielding was placed around the PMT. The photodiode could not be used here because its collecting surface was only 2 mm in diameter, which is not large enough to collect all the light from the BCF-60, whose diameter is 3 mm. For the second measurement, the scintillating fibers were coupled to an optical fiber with a diameter of 1 mm that was connected to the photodiode.

III. RESULTS

A. Comparison of scintillating fiber and plastic scintillator emission spectra

The spectra of all scintillator listed in Table I are shown in Fig. 4. Comparison of the emission peaks to manufacturer data yielded good agreement in every case, as shown in Table II. The total emission intensity was evaluated by integrating the spectra from 375 to 550 nm for the blue scintillators and from 475 to 650 nm for the green scintillators. The results show that the scintillating fiber has wider spectra than

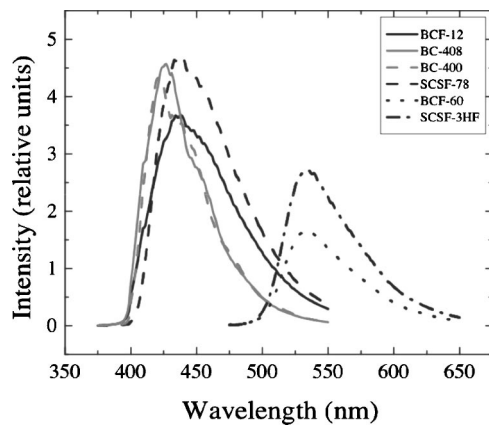


FIG. 4. Experimental measurement of the emission spectra of four scintillating fibers (BCF-12, BCF-60, SCSF-78, SCSF-3HF) and two plastic scintillators (BC-400, BC-408).

plastic scintillator and that more light is collected with the blue scintillating fibers than with the plastic scintillators, even if the peaks of the BC-400 and BC-408 are higher than that of the BCF-12 in Fig. 4. The green emitting fibers are less intense than the others: the light from the BCF-60 is less than 50% of that collected from the BC-400. The best light collection was achieved by the multicladd fibers.

B. Dependency on scintillator length

For a uniform dose, the total light produced inside a volume of scintillating material is proportional to its size, so that increasing either the diameter or the length of the cylindrical probe should increase the signal. However, for long scintillation probes, the light produced at a position far from the coupling interface suffers more attenuation. Moreover, this light has a smaller chance of directly entering the optical fiber than the light produced near the coupling. If there is total reflexion at the wall interface, the photons should be guided from the end toward the light guide at the other end. In this case, Eq. (3) is valid everywhere and the signal must be proportional to the probe length.

The results for measurement of the collected signal as a function of length are presented in Fig. 5 for scintillating fiber and plastic scintillator. Results are normalized to the

signal of maximum length. For both cases the theoretical behavior given by Eq. (3) is shown. It is normalized at the 7 mm fiber length.

As seen in Fig. 5(a), the relation between the collected signal and fiber length for the scintillating fibers is linear for lengths ranging from 1 to 12 mm and shows good agreement with theoretical predictions. However, in Fig. 5(b), the measurements do not show a linear relation between signal and scintillator length and there is no clear agreement between the measured data and the predictions. This can be explained by the fact that there is not always a total reflection at the wall-air interface of the plastic scintillator and some signal is lost. As was suggested in Sec. II A, several factors limit those reflections like damage to the scintillator surface and its surrounding. With their relatively thick cladding, scintillating fibers are more robust and these losses are minimized, resulting in a higher collection efficiency.

C. Dependency on scintillator diameter

Results for the total light produced by a scintillating fiber as a function of the diameter and the light collected by a 1 mm optical fiber (light guide) are presented in Fig. 6. Both graphs are normalized to the value for the 1-mm-diam scintillating fiber.

For a piece of fixed length, its volume is proportional to the squared radius of the fiber. Therefore a quadratic fit was done on the total light collection showing that the total light increased proportionally with the scintillating volume. The quantity of light that is collected by an optical fiber of 1 mm is linear as function of the scintillating fiber radius. The slope of this linear behavior is 1.07.

IV. DISCUSSION

A. On the choice of optimal wavelength and scintillator type

It is clear from Table II that, for a similar spectral range, scintillating fibers provide an advantage over standard scintillators. While both plastic scintillators gave similar results, collected light was 20% greater for the singly clad BCF-12 scintillating fiber illuminated by a 5 mm field of ultraviolet light than for the BC-400 under the same conditions. For the multicladd SCSF-78, the collected signal was 44% higher than for the BC-400.

Many authors have suggested that the stem effect caused by Cerenkov radiation must be reduced in scintillation dosimetry.^{10,11,14,18} For scintillation light within a given wavelength range, there is an undesired Cerenkov contribution proportional to $1/\lambda^3$ in intensity superposed onto the dosimetric signal.¹³ For this reason, even if they produce lower intensity output, green fibers (BCF-60, SCSF-3HF) have been considered as a solution to separate the signal from the main component of Cerenkov radiation that could then be filtered out. By combining the results from Sec. III A and the $1/\lambda^3$ relationship, it is possible to estimate the SNR

TABLE II. Comparison of plastic scintillator and scintillating fibers.

Name	Emission peak		Total emission (norm units)
	Nominal (nm)	Measured (nm)	
SCSF-3HF	530	535	0.77
SCSF-78	450	437	1.44
BCF-60	530	533	0.47
BCF-12	435	438	1.20
BC-400	423	421	1.00
BC-408	425	427	1.05

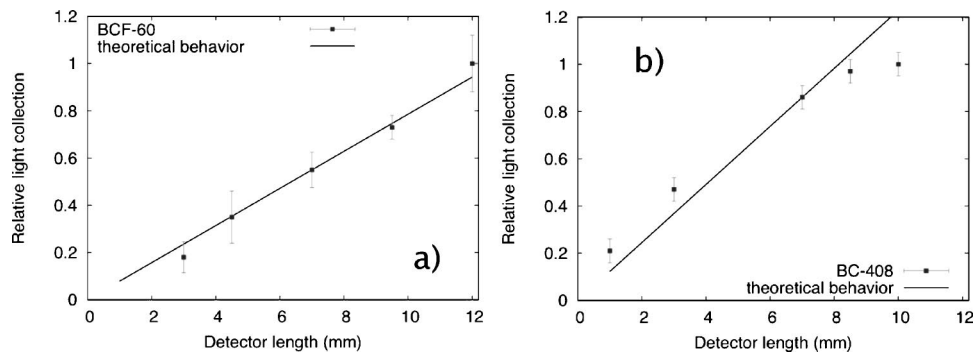


FIG. 5. Light emission of (a) a scintillating fiber (SF; BCF-60) as a function of total length and (b) a plastic scintillator (PS; BC-408). In each case, normalization was done at the 7 mm fiber length.

for the various scintillating materials from Table I. By neglecting all sources of noise except Cerenkov radiation, the SNR can be expressed as

$$\text{SNR} \propto \int_{\lambda_2}^{\lambda_1} \frac{S(\lambda)}{1/\lambda^3},$$

where $S(\lambda)$ is the experimental spectrum from Fig. 4. Figure 7 shows the results from this approximation for the SNR for different bandwidths. Limits of integration for the wavelength range of 175 nm, which is the full bandwidth available, were the same as in Sec. III A. Every other spectral range was considered to be centered on the emission peak (P) of its scintillating material so that the integration limits were $P \pm 175/2$ nm. All points are normalized to the computed SNR of a BC-400 integrated over the whole 175 nm range. It is important to note that Fig. 7 and others thereafter were done with the intensity of scintillation emission and the intensity of Cerenkov effect. To consider the number of photons instead, each point of the intensity curves in Fig. 4 has to be multiplied by their corresponding wavelengths (λ). However, since the Cerenkov is proportional to $1/\lambda^2$ in this case, the results are exactly the same for the intensity and for the total number of photons.

The best SNR is obtained by the two multiclad fibers: the green and the blue. Next best is the BCF-12 scintillating fiber, but since its spectrum shape is more spread out than

those of the two plastic scintillators, its advantage decreases when the total bandwidth is reduced. However, as shown in Fig. 8, reducing the bandwidth considerably diminishes the total collected signal, which could lead to problems with the photodetector sensitivity.

The two graphs (Figs. 7 and 8) were made by using the plastic scintillator and scintillating fiber intensity measured in Sec. III A that was taken for a probe 10 mm long. Shorter scintillator length will cause a reduction in the total scintillation signal, but since the signal decrease for length between 7 and 10 mm is slower for a plastic scintillator than a scintillating fiber (see Fig. 5), the difference between those two types of scintillators will be smaller for smaller length of scintillating material.

The SNR values given in Fig. 7 represent an ideal case. In a real dosimeter, the photodetector has its own nonuniform spectral response (i.e., quantum efficiency) that should be taken into account instead of the flat response for a given bandwidth used here. However the estimate presented in this section is valuable for selecting a photodetector with a spectral response that could lead to an optimal SNR. Moreover, it should be mentioned that Cerenkov radiation is not the only source of noise in a scintillation dosimeter: the photodetector possesses an intrinsic noise that also needs to be considered when making such a selection.

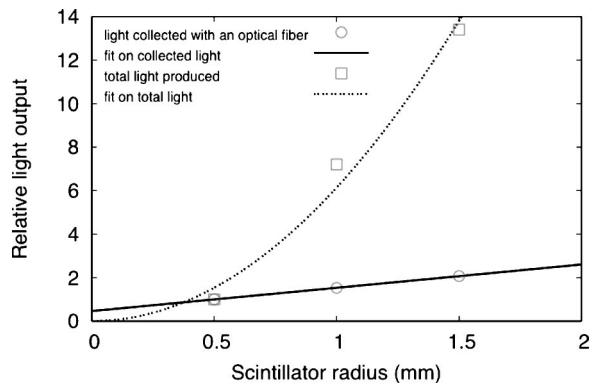


FIG. 6. Light collection as a function of the scintillating fiber radius. Light collected by an optical fiber with a 0.5 mm radius is compared with total light collected directly at the exit of the scintillating fiber. Both results are normalized to those for the 0.5 mm radius scintillating fiber. The error bars are as large as the symbols.

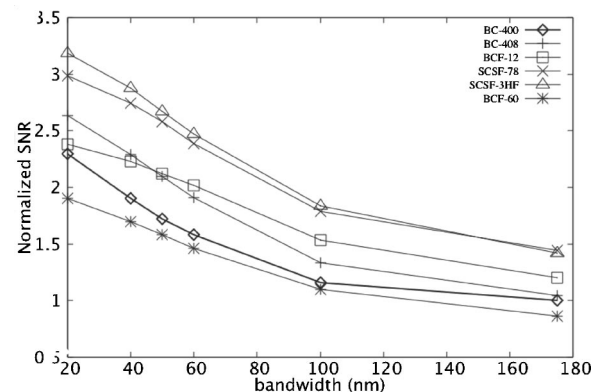


FIG. 7. Estimation of the SNR for all plastic scintillators and scintillating fibers as a function of the total bandwidth on which the signal is accumulated. The scintillation signal is taken from Fig. 5 and the Cerenkov noise intensity is proportional to $1/\lambda^3$.

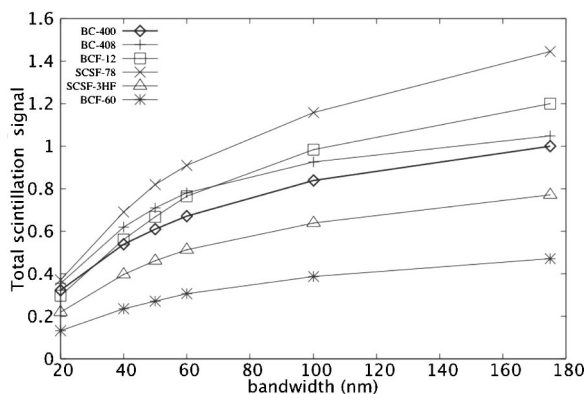


FIG. 8. Total scintillation signal emitted for each kind of scintillator as a function of the total bandwidth used.

B. On the choice of optimal size

Several groups have worked with small volume scintillator dosimeters,^{5-7,24} and each has used different probe sizes. For instance, Fontbonne *et al.* used a cylindrical probe 1 mm in diameter by 10 mm in length,⁷ while Letourneau *et al.* used a probe 1 mm in diameter by 5 mm in length.⁶ Beddar *et al.* used a probe 1 mm in diameter and 2 mm in length, and they used a PMT instead of the photodiodes used by the two other groups.²⁴ To evaluate complex dose patterns like those delivered by IMRT, the detector should be of similar dimensions in every direction (i.e., it should be symmetric). If not, its spatial resolution will vary depending on the direction considered. A cylinder with a 1 mm diameter and a 5 mm length, for example, could detect dose variations occurring over a 2 mm distance only if its length is perpendicular to the gradient.

Since it was shown in Secs. III B and III C that the scintillation signal of a scintillating fiber probe grows linearly with both the scintillating radius and length, one can argue that a cylindrical scintillating fiber probe with a 1 mm diameter and 10 mm length could be replaced by a more symmetric $3 \times 4 \text{ mm}^2$ (3 mm diameter by 4 mm length) scintillating fiber with an emission reaching 80% of the $1 \times 10 \text{ mm}^2$ detector.⁷ A $1 \times 5 \text{ mm}^2$ detector could be replaced by one with $2 \times 3 \text{ mm}^2$ dimensions to obtain an equivalent signal.⁶ The compromise necessary for this improved symmetry is an increased volume: 3.6 times for the $3 \times 4 \text{ mm}^2$ compared to a $1 \times 10 \text{ mm}^2$ detector, and 2.4 times for the $2 \times 3 \text{ mm}^2$ compared to the $1 \times 5 \text{ mm}^2$ detector. The direct consequence of this is a small loss of spatial resolution in one direction. For a plastic scintillator with a length above 7 mm [see Fig. 5(b)], decreasing its volume would result in smaller signal reductions than in the case of a scintillating fiber, however, because of the higher collection efficiency of scintillating fibers, a $3 \times 4 \text{ mm}^2$ probe will still be more efficient if it is made of scintillating fiber.

Increasing the radius of the optical fiber along with the scintillator would increase the total signal as the square of the radius, but it would also increase the Cerenkov light pro-

duced in the collecting fiber. For this reason, it is important to keep the optical fiber radius as small as possible.

C. On the use of scintillation dosimeters in radiotherapy

In radiotherapy, dose precision has always been one of the main concerns for medical physicists. With the advance of complex irradiation schemes such as IMRT and stereotactic radiosurgery, spatial resolution becomes more and more of an issue. Standard ionization chambers are one the best tools to assess absolute dose, but they generally lack good spatial resolution. For this reason, other kinds of dosimeters such as TLD, diodes, and MOSFETs are frequently used to complement measurements made by ionization chambers. In addition to their small sensitive volumes, scintillation dosimeters exhibit the best water equivalence, dose rate linearity, and energy independence down to 125 keV.^{5,9} These advantages, as well as the relatively low cost of these dosimeters, make them good candidates for IMRT plan evaluation and small field dosimetry. Systems using a PMT as a photodetector have been shown to be good candidates for the dosimetry of small radiosurgery fields,²⁴ whereas systems using other photodetectors must have increased SNR if they are to be used widely.

In this paper, several commercial scintillators and scintillating fibers have been compared in terms of their emission spectra and intensities. We found that a careful selection of the scintillating material could increase the SNR and therefore increase the efficiency of the dosimeter. For scintillation in the blue region, the signal intensity of a singly clad scintillating fiber was 120% of that of the plastic scintillator, whereas that of a multiclاد fiber was 144% that of the plastic scintillator. The intensity of green scintillating fibers was lower than that of the plastic scintillator: 47% for the singly clad (BCF-60) fiber and 77% for the multiclاد. Even with this loss of intensity, the SNR of the multiclاد fiber could be increased since Cerenkov radiation, which is the main source of noise, quickly decreases with increasing wavelength. The BCF-60, a singly clad green scintillating fiber, does not provide sufficient intensity to improve the SNR.

With respect to spatial resolution, we studied collected light as a function of length and diameter to find equivalent volumes to asymmetric scintillation probes found in the literature. For instance, a cylinder of 1 mm diameter and 5 mm length can be replaced by a cylinder of 2 mm diameter and 2.5 mm length to obtain the same signal. Even if the more symmetric probe has a total volume two times larger than its longer counterpart, it has nearly the same spatial extent in all directions. Moreover, the $2 \times 3 \text{ mm}^2$ scintillator has a volume of 0.0095 cm^3 , which is of the same order as the smallest ionization chambers commercially available. However, since there is no wall and electrode in a scintillation dosimeter, its total volume is smaller than the total volume of a small ionization chamber.

V. CONCLUSIONS

We have presented a comparison of type, length, and diameter for several types of plastic scintillators and scintillating fibers to guide the choice of optimal scintillator for a small volume dosimeter. We found that scintillating fibers could collect more light than a plastic scintillator with a similar spectral range. With each given photodetector having a known spectral response and quantum efficiency, these comparisons may be used to select the most appropriate scintillating material for the highest possible SNR in order to reduce the impact of stem effect. The increase in signal as a function of diameter and length has also been studied to determine the dimensions of a symmetric detecting volume with the same spatial resolution in every direction.

ACKNOWLEDGMENTS

This work was supported by a scholarship and research grant from the Natural Sciences and Engineering Research Council of Canada (NSERC) and by the Fond Quebecois de la Recherche sur la Nature et les Technologies (FQRNT). The authors would also want to thank professor Réal Vallé and the Centre d'Optique, Photonique et Laser (COPL) for their help with the OSA.

^{a)}Electronic mail: louis.archambault.1@phy.ulaval.ca

¹F. H. Attix, *Introduction to Radiological Physics and Radiation Dosimetry* (Wiley, New York, 1986).

²W. U. Laub and T. Wong, "The volume effect of detectors in the dosimetry of small fields used in IMRT," *Med. Phys.* **30**, 341–347 (2003).

³B. L. Leybovich, A. Sethi, and N. Dogan, "Comparison of ionization chambers of various volumes for IMRT absolute dose verification," *Med. Phys.* **30**, 119–123 (2003).

⁴D. A. Low, P. Parikh, J. F. Dempsey, S. Wahab, and S. Huq, "Ionization chamber volume averaging effects in dynamic intensity modulated radiation therapy beams," *Med. Phys.* **30**, 1706–1711 (2003).

⁵A. S. Beddar, T. R. Mackie, and F. H. Attix, "Water-equivalent plastic scintillation detectors for high-energy beam dosimetry. I. Physical characteristics and theoretical consideration," *Phys. Med. Biol.* **37**, 1883–1900 (1992).

⁶D. Letourneau, J. Pouliot, and R. Roy, "Miniature scintillating detector for small field radiation therapy," *Med. Phys.* **26**, 2555–2561 (1999).

⁷J. M. Fontbonne, G. Iltis, G. Ban, A. Battala, J. C. Vernhes, J. Tillier, N. Bellaize, C. LeBrun, B. Tamain, K. Mercier, and J. C. Motin, "Scintillating fiber dosimeter for radiation therapy accelerator," *IEEE Trans. Nucl. Sci.* **49**, 2223–2227 (2002).

⁸H. Perera, J. F. Williamson, S. Monthofer, W. R. Binns, J. Klarman, G. L. Fuller, and J. W. Wang, "Rapid two-dimensional dose measurement in brachytherapy using plastic scintillator sheet: Linearity, signal to noise ratio and energy response characteristics" *Int. J. Radiat. Oncol., Biol., Phys.* **23**, 1059–1069 (1994).

⁹A. S. Beddar, T. R. Mackie, and F. H. Attix, "Water-equivalent plastic scintillation detectors for high-energy beam dosimetry. II. Properties and measurements," *Phys. Med. Biol.* **37**, 1901–1913 (1992).

¹⁰A. S. Beddar, T. R. Mackie, and F. H. Attix, "Cerenkov light generated in optical fibres and other light pipes irradiated by electron beams," *Phys. Med. Biol.* **37**, 925–935 (1992).

¹¹M. A. Clift, R. A. Sutton, and D. V. Webb, "Dealing with Cerenkov radiation generated in organic scintillator dosimeter by bremsstrahlung beams" *Phys. Med. Biol.* **45**, 1165–1182 (2000).

¹²M. Westermark, J. Arndt, B. Nilsson, and A. Brahme, "Comparative dosimetry in narrow high-energy photon beams," *Phys. Med. Biol.* **45**, 685–702 (2000).

¹³J. V. Jelley, *Cerenkov Radiation and its Applications* (Pergamon, New York 1958).

¹⁴S. F. Boer, A. S. Beddar, and J. A. Rawlinson, "Optical filtering and spectral measurement of radiation-induced light in plastic scintillator dosimetry," *Phys. Med. Biol.* **38**, 945–958 (1993).

¹⁵M. A. Clift, R. A. Sutton, and D. V. Webb, "Water equivalence of plastic organic scintillator in megavoltage radiotherapy bremsstrahlung beams," *Phys. Med. Biol.* **45**, 1885–1895 (2000).

¹⁶K. J. Jordan, "Evaluation of ruby as a fluorescent sensor for optical fiber-based radiation dosimetry," *Proc. SPIE* **2079**, 170–178 (1996).

¹⁷B. L. Justus, P. Falkenstein, A. L. Huston, M. C. Plazas, H. Ning, and R. W. Miller, "Gated fiber-optic-coupled detector for *in vivo* real-time radiation dosimetry," *Appl. Opt.* **43**, 1663–1668 (2004).

¹⁸M. A. Clift, P. N. Johnston, and D. V. Webb, "A temporal method of avoiding the Cerenkov radiation generated in organic scintillator dosimeters by pulsed mega-voltage electron and photon beams," *Phys. Med. Biol.* **47**, 1421–1433 (2002).

¹⁹A. S. Beddar, "A new scintillator detector system for the quality assurance of ⁶⁰Co and high-energy therapy machines," *Phys. Med. Biol.* **39**, 253–263 (1994).

²⁰J. Indra, M. J. Gazda, and A. S. Beddar, "Characteristics of a scintillator-based daily quality assurance device for radiation oncology beams" *Med. Phys.* **23**, 2061–2067 (1996).

²¹A. S. Beddar, S. Law, N. Suchowerska, and T. R. Mackie, "Plastic scintillation dosimetry: Optimization of light collection efficiency," *Phys. Med. Biol.* **48**, 1141–1152 (2003).

²²V. Hagopian and I. Daly, *Radiation Damage on Fibers*, SciFi97: Workshop on Scintillating Fibers Detectors (Springer, Berlin, 1998), pp. 53–61.

²³T. O. White, "Scintillating fibres," *Nucl. Instrum. Methods Phys. Res. A* **273**, 820–825 (1988).

²⁴A. S. Beddar, T. J. Kinsella, A. Ikhlef, and C. H. Sibata, "A miniature 'scintillator-fiberoptic-PMT' detector system for the dosimetry of small fields in stereotactic radiosurgery," *IEEE Trans. Nucl. Sci.* **48**, 924–928 (2001).

ORIGINAL RESEARCH

Open Access



Estimating relationship between the time over threshold and energy loss by photons in plastic scintillators used in the J-PET scanner

S. Sharma^{1*} , J. Chhokar¹, C. Curceanu², E. Czerwiński¹, M. Dadgar¹, K. Dulski¹, J. Gajewski³, A. Gajos¹, M. Gorgol⁴, N. Gupta-Sharma⁴, R. Del Grande², B.C. Hiesmayr⁵, B. Jasińska⁴, K. Kacprzak¹, Ł. Kapłon¹, H. Karimi¹, D. Kisielewska¹, K. Klimaszewski⁶, G. Korcyl¹, P. Kowalski⁶, T. Kozik¹, N. Krawczyk¹, W. Krzemień⁷, E. Kubicz¹, M. Mohammed^{1,9}, Sz. Niedźwiecki¹, M. Pałka¹, M. Pawlik-Niedźwiecka¹, L. Raczyński⁶, J. Raj¹, A. Ruciński³, Shivani¹, R.Y. Shopa⁶, M. Silarski¹, M. Skurzok^{1,2}, E.Ł. Stępień¹, W. Wiślicki⁷, B. Zgardzińska⁴ and P. Moskal¹

*Correspondence:

sushil.sharma@uj.edu.pl

¹ Faculty of Physics, Astronomy and Applied Computer Science, Jagiellonian University, prof. Stanisława Łojasiewicza 11, 30-348 Cracow, Poland

Full list of author information is available at the end of the article

Abstract

Purpose: The time-over-threshold (TOT) technique is being used widely due to its implications in developing the multi-channel readouts, mainly when fast signal processing is required. Using the TOT technique, as a measure of energy loss instead of charge integration methods, significantly reduces the signal readout costs by combining the time and energy information. Therefore, this approach can potentially be utilized in J-PET tomograph which is built from plastic scintillators characterized by fast light signals. The drawback in adopting this technique lies in the non-linear correlation between input energy loss and TOT of the signal. The main motivation behind this work is to develop the relationship between TOT and energy loss and validate it by the J-PET tomograph setup.

Methods: The experiment was performed using a ²²Na beta emitter source placed in the center of the J-PET tomograph. This isotope produces photons of two different energies: 511 keV photons from the positron annihilation (direct annihilation or through the formation of a para-positronium atom or pick-off process of ortho-positronium atoms) and a 1275 keV prompt photon. This allows the study of the correlation between TOT values and energy loss for energy ranges up to 1000 keV. Since the photon interacts predominantly via Compton scattering inside the plastic scintillator, there is no direct information of the energy deposition. However, using the J-PET geometry, one can measure the scattering angle of the interacting photon. Since the ²²Na source emits photons of two different energies, it is necessary to know unambiguously the energy of incident photons and their

(Continued on next page)

(Continued from previous page)

corresponding scattering angles in order to estimate energy deposition. In summary, this work presents a dedicated algorithm developed to tag photons of different energies and studying their scattering angles to calculate the energy deposition by the interacting photons.

Results: A new method was elaborated to measure the energy loss by photons interacting with plastic scintillators used in the J-PET tomograph. We find the relationship between the energy loss and TOT is non-linear and can be described by the functions $TOT = A0 + A1 * \ln(E_{dep} + A2) + A3 * (\ln(E_{dep} + A2))^2$ and $TOT = A0 - A1 * A2^{E_{dep}}$. In addition, we also introduced a theoretical model to calculate the TOT as a function of energy loss in plastic scintillators.

Conclusions: A relationship between TOT and energy loss by photons interacting inside the plastic scintillators used in J-PET scanner is established for a deposited energy range of 100–1000 keV.

Keywords: Positron emission tomography, Time over threshold, Positronium atoms, Medical imaging

Background

The time-over-threshold (TOT) technique was first time introduced by Nygren and Millaud [1] and proved to be an excellent solution for multi-channel readouts [2]. In the TOT method, one measures the signal pulse width at a selected threshold, which can be used to estimate the signal's charge. For energy deposition estimation, this method is less precise in comparison to the charge integration method. However, it reduces the readout costs by using only the time to digital converter (TDC), herewith combining both timing and energy information. The application of the TOT method for the energy loss determination may be of particular advantage in the newly developed Jagiellonian-positron emission tomograph (J-PET) [3, 4] which is based on plastic scintillators characterized by fast light signals with rise and decay times of the order of ≈ 1 ns [5, 6] and thus being about two orders of magnitude shorter than signals from crystals used in the current PET devices [7–9]. Therefore, the application of the TOT method for PET tomographs built from plastic scintillators will enable fast signal processing and significantly reducing signal acquisition dead time with respect to the crystal based tomographs. Despite many advantages like compactness of signals readout and low power consumption, the TOT technique confronts the challenge in terms of non-linear input energy to pulse width conversion [10–12]. It has been reported that using multiple fixed triggering thresholds [13, 14] or dynamic threshold levels [15, 16] for estimating the TOT values alleviates the problem of non-linearity to a significant extent.

In PET applications, the precise determination of the photon's interaction position, hit time, and energy loss is crucial. Currently, in PET scanners, crystal scintillators are used and they enable the determination of the energy of the interacting photons as they undergo photoelectric effect [17–19]. In contrast to crystals in plastic scintillators, the incident photon interacts via Compton scattering depositing only part of its energy. Thus, there is no direct information on the energy deposition of the interacting photon.

TOT studies with plastic scintillators are very scarce [20]. In the recent work of Ashrafi and Gol [21], the energy calibration of a plastic scintillator based on Compton scattering and observing the light yield by using various monochromatic photon sources was

reported. In this work, we take advantage of the multilayer cylindrical acceptance of the J-PET scanner [3, 22] which allows us to determine the direction of the photon before and after the scattering which in turn gives us access to its scattering angle [4, 23]. Thus, knowing the incident energy and the measured scattering angle of the initial photon, the deposited energy in the photon's interaction can be calculated [24].

For the present study, a ^{22}Na source was used which emits photons of two different energies: 511 keV (annihilation) and 1275 keV (prompt). The 511 keV photons originate from the direct electron-positron annihilation, from the decay of para-positronium, and from the annihilation of ortho-positronium atoms via the pick-off processes [25–27]. Since the aim of the study is to establish the relationship between TOT and energy loss, we need to develop an algorithm capable to clearly distinguish between the annihilation and prompt photons as well as a method of proper correspondence of the measured signals to the initial and scattered photons. To achieve this, we performed studies based on the assumptions that 511 keV photons emitted in the annihilation of e^+e^- are always back-to-back due to momentum conservation. Secondly, to identify the prompt photons, we take advantage of the decay of long-lived ortho-positronium atoms [28] which in the XAD-4 porous polymer [29] on the average decay about 90 ns after the emission of a prompt photon. In this article, the presented algorithm allows us for establishing a relationship between TOT and energy deposition in plastic scintillators, a step further towards medical imaging with low cost PET devices.

Methods

The Jagiellonian-positron emission tomograph (J-PET) consists currently of 192 plastic scintillators made of EJ-230 material. A single detection module is composed of a scintillator with dimension $0.7 \times 1.9 \times 50 \text{ cm}^3$ connected with a R9800 Hamamatsu photomultiplier on each side [30, 31]. The detection modules are axially arranged in three layers: the first and second layer are composed of 48 modules whereas the third layer is the arrangement of 96 modules. Layers are not overlaying and have a diameter of 85 cm, 93.5 cm, and 115 cm, respectively. The front view of three layer prototype of the J-PET scanner is shown in Fig. 1a whereas Fig. 1b exhibits its cross section. A Multi-Voltage Threshold mezzanine (MVT) board is used to probe signals at four fixed thresholds (80, 160, 240, and 320 mV) in the voltage domain (within the accuracy of 20 ps RMS) [32] to achieve the good resolution of determining the hit time and place of interaction of photon inside the scintillator [3, 31, 33–35]. Using MVT boards connected to readouts allows us to exploit the FPGAs differential inputs as comparators. The signals from the MVT boards are sampled using TDCs implemented in the FPGA devices [36–39] whereas in standard approach, external comparator chips are used additionally [40, 41]. The data is stored in a trigger less mode with an ability to handle the data stream with rates of about 8 Gbps [42, 43]. The position of interaction along the plastic strip is calculated based on the time difference of light signals arriving at both photomultipliers. The hit-time resolution for the registration of 511 keV photon is $\approx 155 \text{ ps}$ [30] whereas the spatial resolution on xy is 4–5 mm and on z-axis is $\approx 25 \text{ mm}$ [44]. Signals from the plastic scintillators are very fast (rise time $\approx 0.5 \text{ ns}$, fall time $\approx 1.8 \text{ ns}$) [6] and are prone to much lower pile-ups with respect to crystal based detectors with an order of magnitude larger fall times [45]. Therefore, in order to avoid additional dead times in the detection system, instead of direct charge measurement only timing of the signal is used. This allows us to handle higher

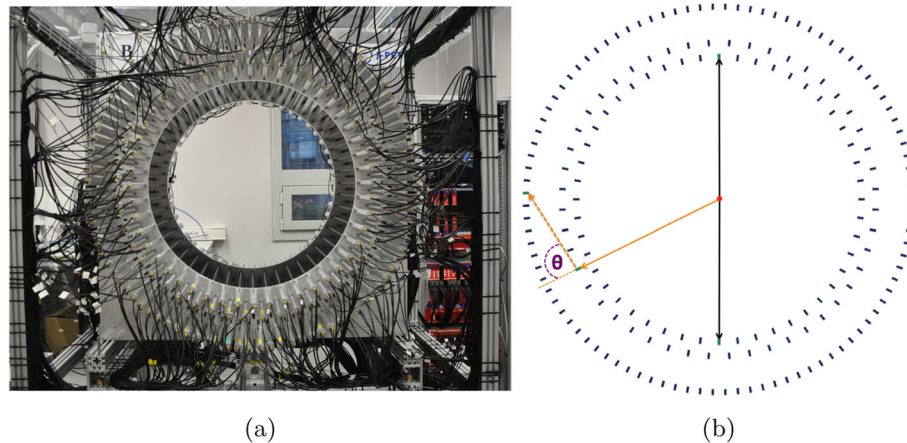


Fig. 1 **a** The photo of J-PET scanner with the front view (see text for description). **b** The cross section of J-PET with superimposed arrows depicting the interaction of 511 keV photons (black solid arrows) originating from positron-electron annihilation and prompt photon 1275 keV before (orange solid arrow) and after (orange dashed arrow) scattering inside the scintillator. Red dot in the center represents the ^{22}Na source

rates of data collection. The photon's interaction in the scintillator and the arrival time of the signals in photomultipliers at each end is measured. The TOT approach is adopted instead of the charge integration method. In TOT approach, the time difference between the leading and trailing edge of signal pulse crossing the applied thresholds is measured. The schematic presentation is shown in Fig. 2. The total TOT, used as a measure of the energy deposition, is estimated as a sum of TOT values measured for all thresholds at both sides of scintillator (Eq. 1):

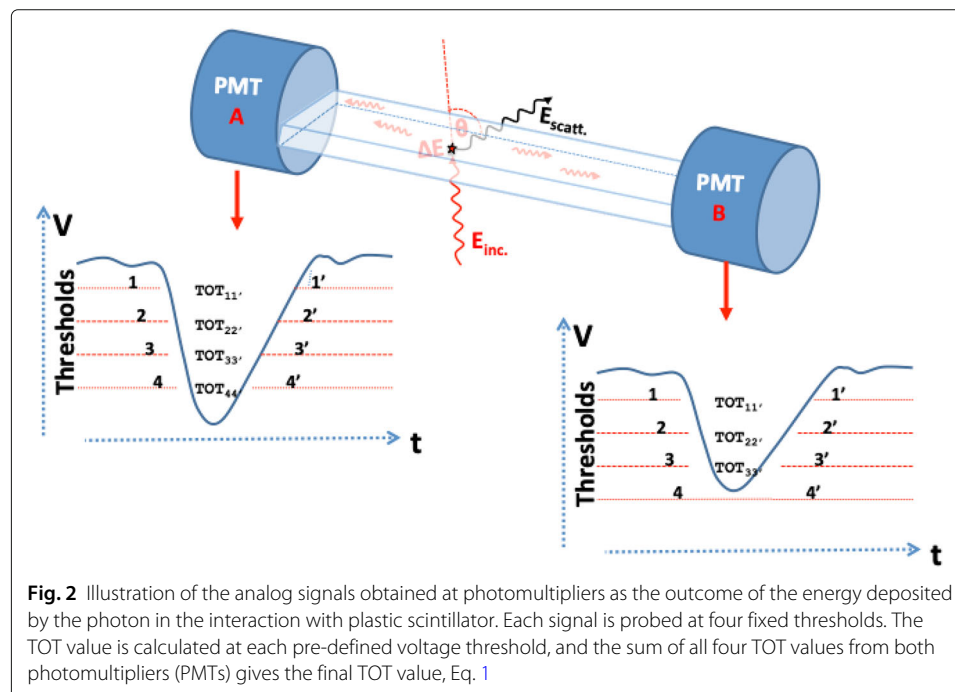


Fig. 2 Illustration of the analog signals obtained at photomultipliers as the outcome of the energy deposited by the photon in the interaction with plastic scintillator. Each signal is probed at four fixed thresholds. The TOT value is calculated at each pre-defined voltage threshold, and the sum of all four TOT values from both photomultipliers (PMTs) gives the final TOT value, Eq. 1

$$TOT = \sum_{PMT=A,B} \sum_{Thr_1-4}^{TOT_{PMT,Thr}} \quad (1)$$

where $TOT_{PMT,Thr}$ is representing the sum of TOT values over all four threshold on the signals measured from both photomultipliers of each scintillator. The estimation of the charge collection using the pulse width of the signal is less precise and suffers a strongly non-linear relationship between TOT and energy deposition. The plastic scintillators are composed of hydrocarbons with low atomic (Z) number; consequently, gamma photons interact in the plastic scintillators predominantly through Compton scattering and deposit only part of their energy. The information of the deposited energy is important to reduce the scatter fraction by requiring that the energy loss is larger than 200 keV [3, 23, 34]. To process the measured data, a dedicated framework for offline data analysis was used [46, 47].

Experimental set-up

The measurements were performed with a ^{22}Na source (1 MBq activity) wrapped inside a very thin Kapton foil. The experimental set-up is shown in Fig. 3. The left panel shows a picture of the J-PET tomograph with the placement of a barrel shape source holder of length ≈ 14 cm and diameter ~ 3.16 cm (at the center). The source surrounded by the porous material was put inside a small chamber of thin layer made of aluminum and placed at the center of the holder (see the upper inset of right panel in Fig. 3). The placement of the source covered with porous material is shown at the lower right insets. In this experiment, the XAD-4 polymer was used which increases the probability of formation of positronium (Ps) atoms [29]. Using the ^{22}Na source gives a possibility to estimate the lifetime of the Ps atom by registering the annihilation photons and prompt gamma which is a feature that will allow a novel application in medical imaging. J-PET is optimized to register multiple photons simultaneously, and thus, it can be used to reconstruct the image of average lifetime of the ortho-positronium ($o\text{-Ps} \rightarrow 3\gamma$) which is formed in patient body during the PET scanning process. The average lifetime of $o\text{-Ps}$ strongly depends on the

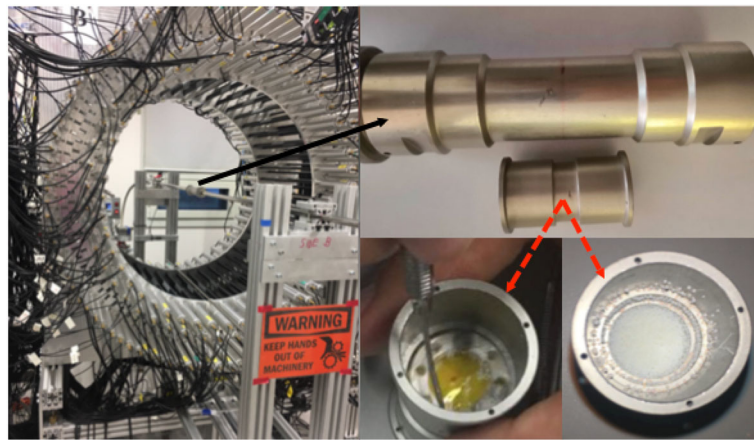


Fig. 3 Experimental set-up of the annihilation chamber with the source placed at the center of the J-PET tomograph

free volume between atoms and thus can be used as a diagnostic indicators of human tissues [26, 27]. In the decay of ^{22}Na source (Fig. 4a), the positron is emitted leaving behind an excited state of ^{22}Ne nucleus which eventually de-excites via the emission of a prompt photon on average within the time interval of ≈ 3.7 ps. The time difference between the interaction of annihilation and prompt photons is then with a very good approximation equal to lifetime of Ps atom [26]. Gamma photons mainly interact inside the plastic scintillator via Compton scattering.

Figure 4b shows the TOT spectrum for all registered photons. The clear Compton edges are visible at about 22 ns and 46 ns corresponding to 511 keV and 1275 keV photons, respectively. The observed enhancement of contributions for the lower values of TOT (below 10 ns) is from the interaction of scattered photon and photons originating from the 3-photon decay of o-Ps atoms. It is worth to emphasize that TOT values could be used to disentangle between the annihilation and prompt photons to some extent. However, in the overlapping region for TOT values below 30 ns, the identification would be ambiguous. Therefore, we developed a dedicated algorithm to uniquely identify the photons of energies 511 keV and 1275 keV irrespective of the TOT values (described in the “Events selection” section). Furthermore, the registration of initial and scattered photons allows us to determine the scattering angle θ (see Fig. 5). Knowing the energy (E_{inc}) and scattering angle (θ) of the initial photon give access to energy deposition ΔE inside the scintillator [24]:

$$\Delta E = E_{inc} \left[1 - \frac{1}{1 + \frac{E_{inc}}{511 \text{ keV}} (1 - \cos \theta)} \right] \quad (2)$$

Determination of ΔE and the measurement of TOT enables to establish the relation between these two variables.

In this work, events with three interactions were studied, assuring that all three hits forming the events are occurring in distinct scintillators. Furthermore, a photon interaction inside the scintillator is termed as hit. The required information (E_{inc}, θ) can be extracted based on two hits only. However, the third hit allows event categorization in a way that we can differentiate the photons of different energies and conjecture their origins.

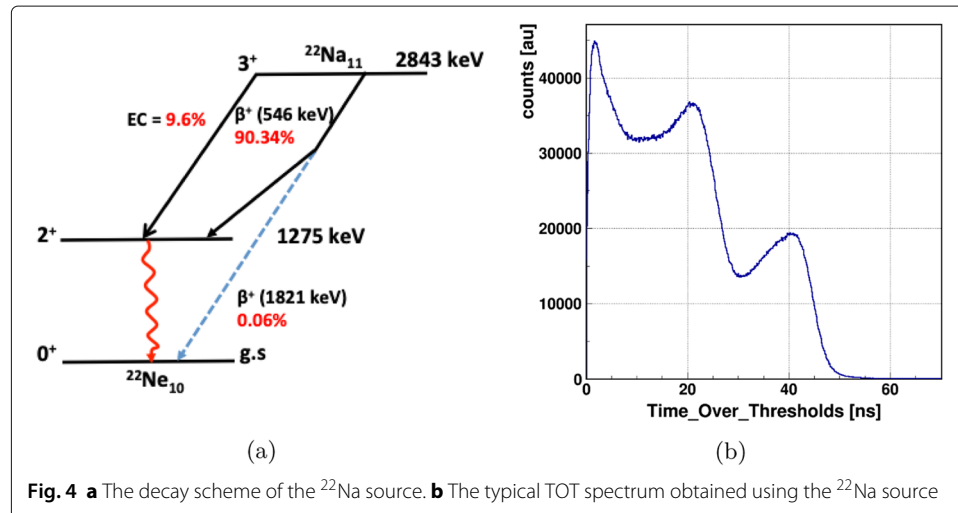
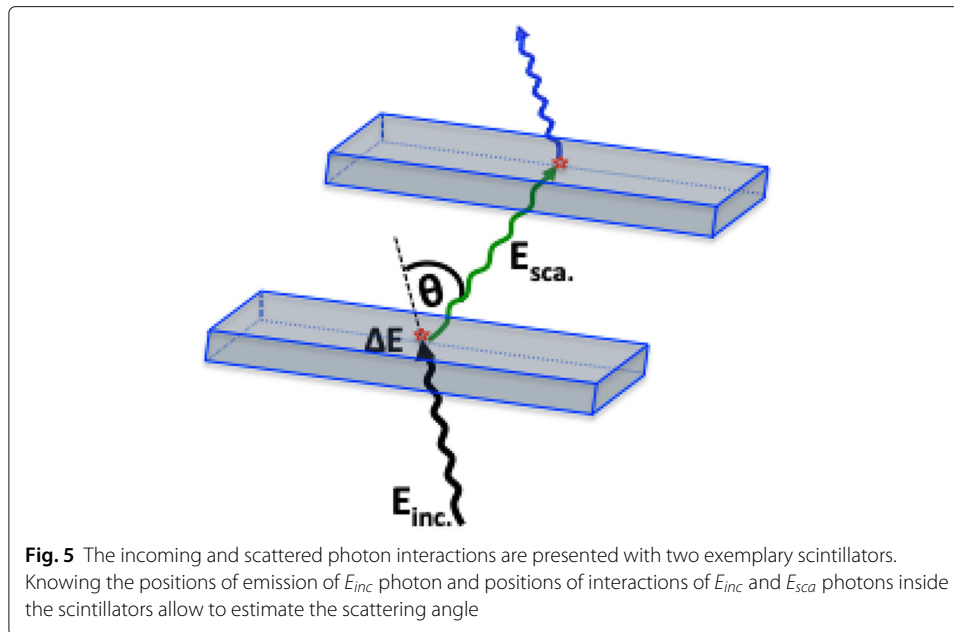


Fig. 4 **a** The decay scheme of the ^{22}Na source. **b** The typical TOT spectrum obtained using the ^{22}Na source

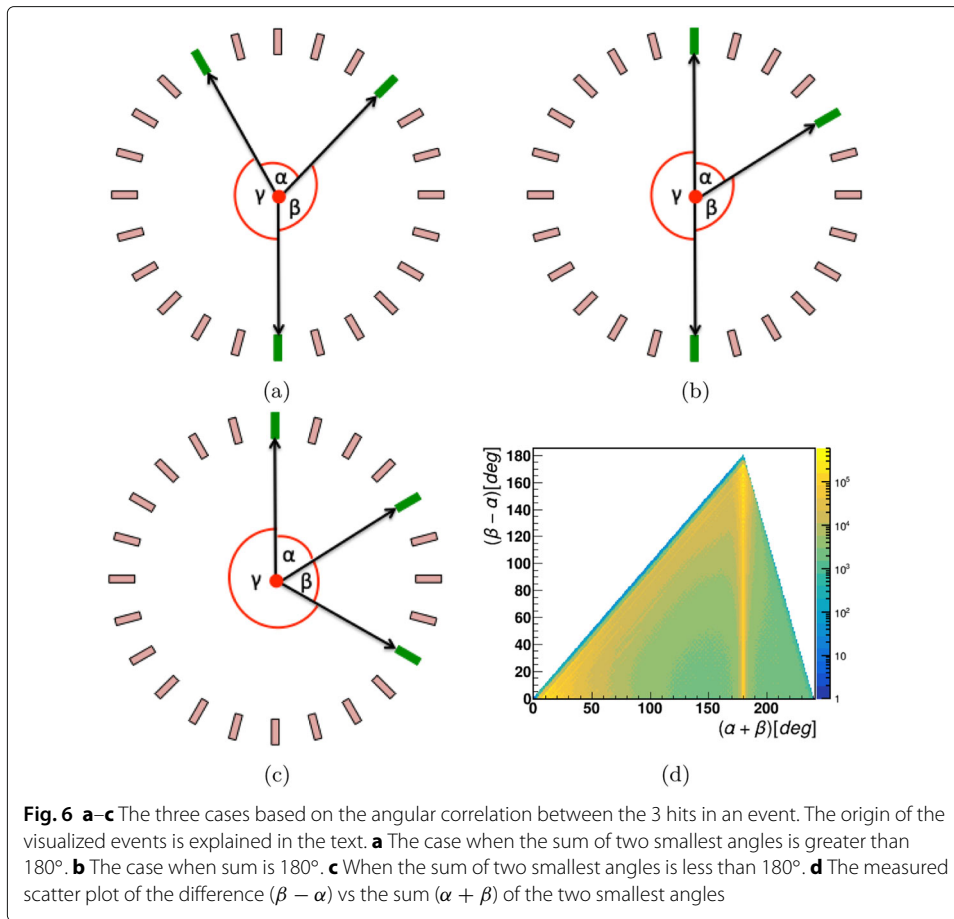


Events selection

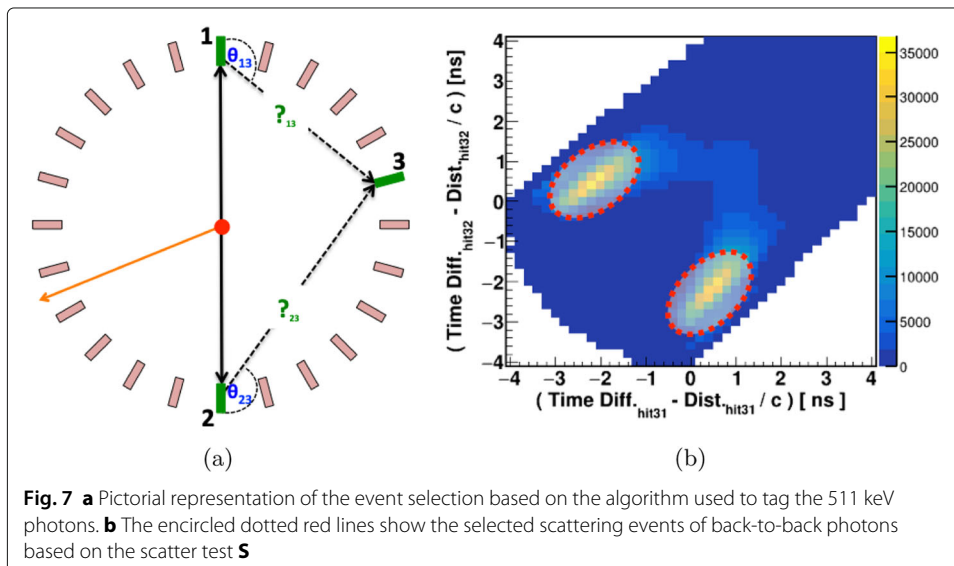
In this analysis, we first select the events containing three hits only. The angular correlations between the registered photons in three hit events can be used to partially identify the origin and energy of photons [48, 49]. A pictorial view of the three hits (green rectangles) and their angular correlations are presented in Fig. 6a–c. For clarity, only a few scintillators mimicking one layer of J-PET scanner are shown. The angles between three hits ordered from the smallest to the largest are α , β , and γ , respectively. The measured sum of the two smallest angles vs their difference is shown in Fig. 6d which shows three distinct regions: (i) $(\alpha + \beta) > 180^\circ$, electron-positron annihilation into three photons originating from direct e^+e^- annihilation or from the decay of o-Ps atoms; (ii) $(\alpha + \beta) = 180^\circ$, two back-to-back photons originating either from direct e^+e^- annihilation or from the decay of p-Ps atom (singlet state of Ps) or from the pick-off of o-Ps; (iii) $(\alpha + \beta) < 180^\circ$, one or two of the hits are from scattering of initial photon or prompt photon. The coincidence time window for an event was fixed at 200 ns in the analysis.

Identification of 511 keV photons

The 511 keV photons are the outcome of e^+e^- annihilation into the back-to-back direction to satisfy the momentum conservation and can easily be identified in Fig. 6d as a vertical line at $\alpha + \beta = 180^\circ$. The selection of such events was done based on the condition that the sum of the two smallest angles ($\alpha + \beta$) should be 180° within the uncertainty of 2° . The pictorial presentation of J-PET with one layer is used to visualize the situation. In Fig. 7a, black lines represent the back-to-back photons labeled as 1 and 2 and the orange line shows the prompt photon. Scintillators with photon hits are shown as green rectangles. Hit 3 corresponds to the interaction of the scattered photon after hit 1 or hit 2. The exact assignment of the scattering photons to its primary one is important for the proper estimation of scattering angle (Fig. 7b) which is essential for the determination of the energy deposition. For this purpose, a scatter test **S** is devised which estimates the



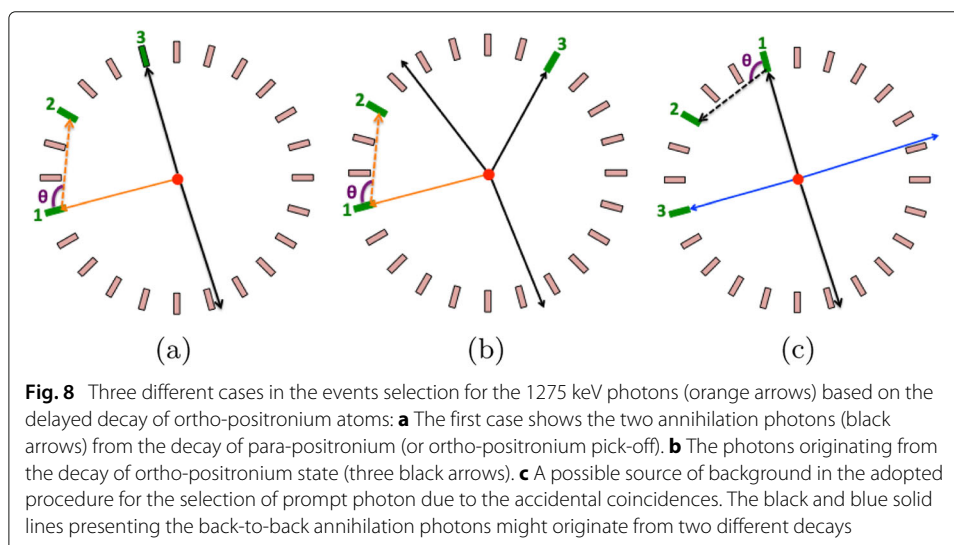
time difference between the measured time (time difference between two hits) and calculated time (distance between hit-positions divided by the speed of light). The S test was applied event-wise assuming both possibilities that the third hit might belong to the scattering photon after hit 1 or hit 2. The results are shown in Fig. 7b. In case of the proper assignment, the value of S should be close to zero. For the final analysis, events from the

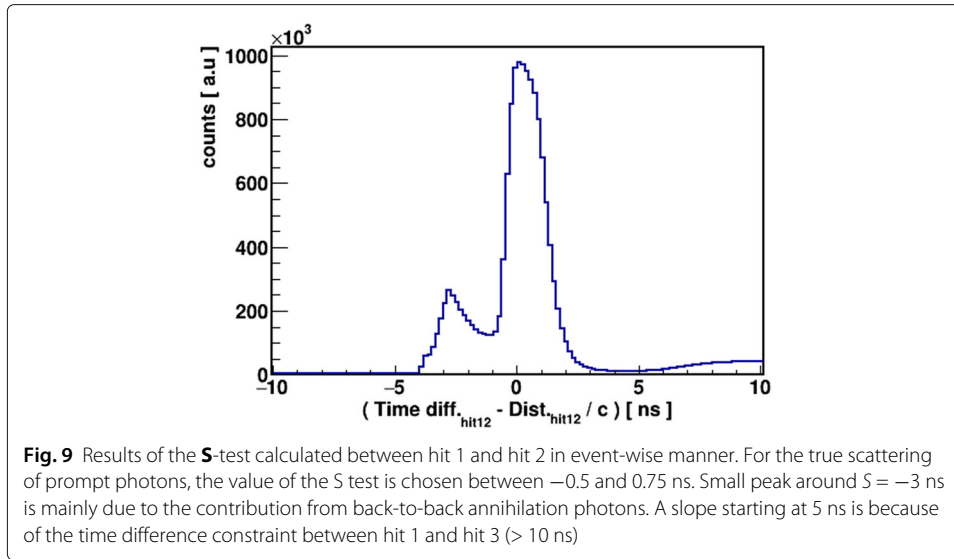


areas encircled by red-dotted lines were taken into account. With the known incident photon's energy (511 keV) and its scattering angle, the deposited energy is calculated in response to the initial hit. Thus, a one-to-one correspondence of energy deposition by 511 keV photons and TOT values on event-wise bases is extracted. In studying 511 keV photons, the relationship can be established only up to 340 keV of energy deposition (the Compton edge for 511 keV photon). So, in order to extend the relationship for higher energy deposition values, the studies with the prompt photons with energy 1275 keV were also performed. The selection criterion for the prompt gamma is explained in the next sub-section.

Identification of 1275 keV photons and their scatterings

The selection of prompt and its corresponding scatter photon without using an explicit cut on TOT values is not as straightforward as in the case of annihilation photons. As the first step in the selection procedure, in order to suppress events with back-to-back 511 photons, we applied cuts based on the angular correlation between the hits (Fig. 6d) such that we are not considering those events when the sum of two smallest angles lies in interval $165\text{--}185^\circ$. In the next step, hits are ordered according to the ascending time and only those events are selected for which the time interval between first and third hit is larger than 10 ns. The assumed analogy is as follows: hit 1 is considered to be the prompt photon, hit 2 is the scattered photon of the prompt, and hit 3 is assumed by one of the photons originating from pick-off (Fig. 8a) or direct from the decay of ortho-positronium atoms (Fig. 8b). Figure 8c shows the possible background in the adopted selection criterion. The time difference (Δt) between the first and third hit is used as a key parameter. It is chosen to be much larger than the possible time difference between the scatterings of photon in the tomograph. For the present analysis, the value for Δt was fixed in the time interval (10–100 ns). For estimating the scattering angles of prompt gamma, the scattered test was applied between first and second hit. The histogram used for the scatter test is shown in Fig. 9. The acceptance time window for the true scattering of the S test is chosen between -0.5 and 0.75 ns.





Theoretical model

The energy deposition by a photon inside a plastic scintillator is a function of scattering angle. Furthermore, the shape and amplitude of the signal pulse vary depending on the properties of scintillators (solvent, solute, and wavelength shifter) [50, 51]. The time distribution spectra of the emitted light in plastic scintillators EJ-230 (Eljen Technology) due to an incoming photon interaction at time Θ can be estimated by the following equation [3, 50, 51]:

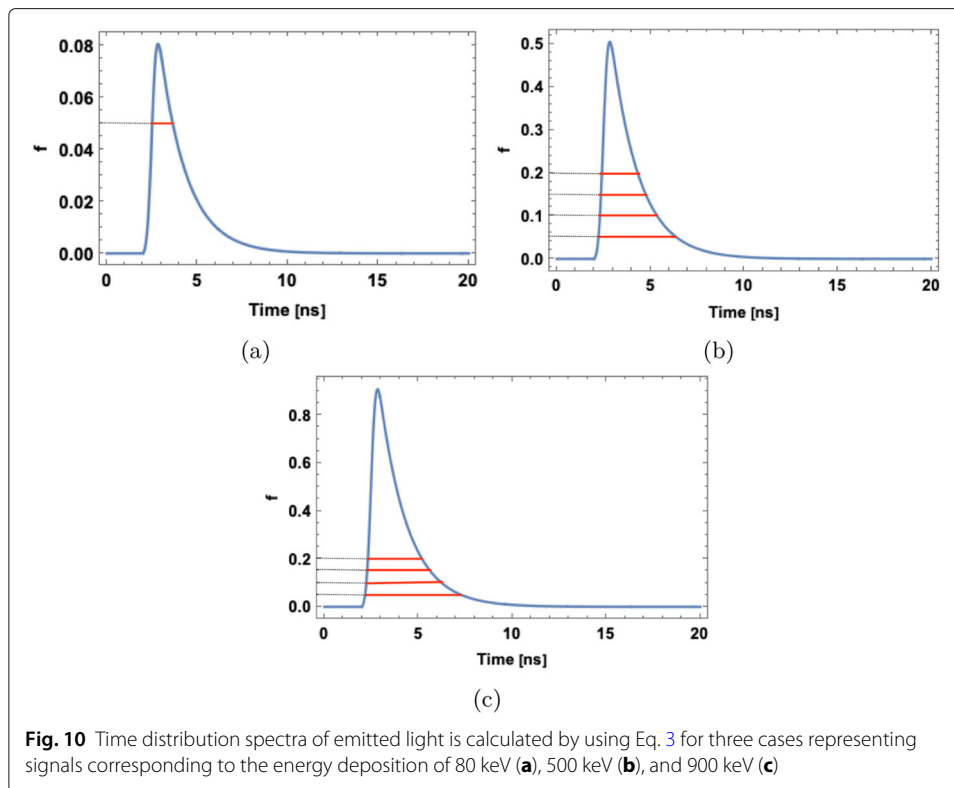
$$f(t|\Theta) = K \int_{\Theta}^t \left(e^{-\frac{t-\tau}{t_d}} - e^{-\frac{t-\tau}{t_r}} \right) \cdot e^{-\frac{(\tau-\Theta-2.5\sigma)^2}{2\sigma^2}} d\tau \quad (3)$$

The equation is a convolution of Gaussian and exponential terms, where σ represents the rate of energy transfer to the primary solute, whereas t_r and t_d denote the average time of the energy transfer to the wavelength shifter and decay time of the final light emission, respectively [51]. K is the normalization factor to unity. At time $\Theta = 2$ ns, $t_d = 1.5$ ns, $t_r = 0.005$ ns, and $\sigma = 0.2$ ns, Eq. 3 gives the time distribution spectra of emitted photons where the deposited energy is characterized by the amplitude of the signal (f). Figure 10 indicates three exemplary pulses calculated according to Eq. 3 normalized relatively to simulate signals corresponding to energy loss of 80 keV (Fig. 10a), 500 keV (Fig. 10b), and 900 keV (Fig. 10c).

Each signal pulse is probed at four thresholds (f) 0.05 (TOT_1), 0.10 (TOT_2), 0.15 (TOT_3), and 0.20 (TOT_4) shown by the red solid lines in Fig. 10. The total TOT value is calculated as $TOT_{model} = N_0 \cdot TOT_{sum}$, where $TOT_{sum} = TOT_1 + TOT_2 + TOT_3 + TOT_4$ and N_0 is a free parameter. The theoretical predictions will be compared with experimental results in the next section.

Results

The motivation of this work is the elaboration of a method to estimate the energy loss by incident photons interacting with plastic scintillators used in the J-PET tomography scanner. The analysis is performed with the ^{22}Na isotope because it is long lived (2.6 years half



lifetime) and is emitting positrons annihilating to 511 keV photons as used in PET diagnostics. Since the aim of this study is to establish the relation between TOT and ΔE for the plastic scintillators, in order to avoid the biasness in identification of 511 keV (positron annihilation) and 1275 keV (deexcitation) photons, a new method of photon identification was developed which is independent of the TOT values. After selecting the photons of different energies, their scattering angles are estimated based on the hit characteristics. With information of incident energy of photon and its scattering direction, the energy transfer to the electrons inside the scintillator can be calculated using the Compton scattering formula (Eq. 2).

In each event, hit characteristics are measured that comprise the TOT values and photon's interaction time as well as spatial coordinates. For all selected hits, the relationship between measured TOT values and the estimated energy deposition is presented in Fig. 11. An enhancement in TOT values is observed with increasing energy depositions which is an expected behavior. However, some contributions are visible with large energy deposition but with smaller TOT values; this can be interpreted as wrongly tagged photons due to accidental coincidences, i.e., instead of 1275 keV photon, photons with lower incident energies were used to estimate the energy deposition for the scattering angles. (e.g., see the Fig. 8c). The accidental coincidence rate for the presented analysis is estimated $\approx 5\%$. The black line in Fig. 11a is plotted by assuming that the wrongly tagged photons are of energy 511 keV. For the final relationship, the profile histograms of Fig. 11a for the most populated energy bins are selected. The TOT spectra for selected energy intervals fitted for a fixed range around the maximum of distribution. The mean values of the TOT distributions as a function of the center value of the energy interval are shown

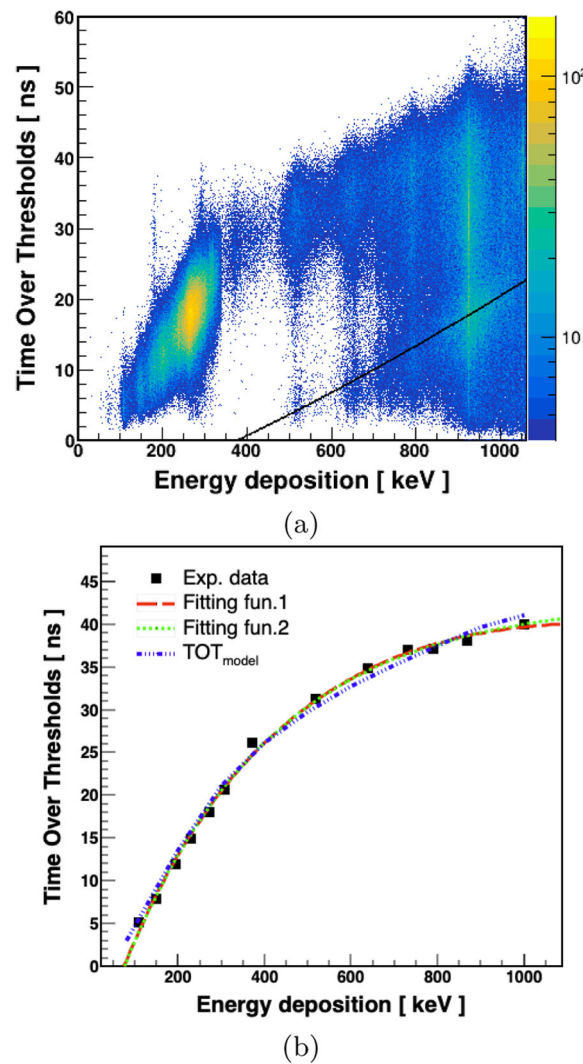


Fig. 11 **a** 2-D spectrum of TOT versus energy deposition. **b** TOT vs energy deposition. Black rectangles correspond to the experimental data. The statistical errors in measuring the values are smaller than the size of symbols due to the large number of entries for the fitted TOT distributions. The red dashed line indicates result of the fit of the function: $TOT = A_0 + A_1 * \ln(E_{dep} + A_2) + A_3 * (\ln(E_{dep} + A_2))^2$, with $A_0 = -2322$ ns, $A_1 = 632.1$ ns/keV, $A_2 = 590.2$ keV, and $A_3 = -42.29$ ns/(keV)². Green dotted line shows the result of another fitting function $TOT = A_0 \text{ ns} - A_1 * A_2^{E_{dep}}$ with three parameters where $A_0 = 42.96$ ns, $A_1 = 53.43$ ns, and $A_2 = 0.997$ keV⁻¹. Blue dotted-dashed line represents the model predictions (the “Theoretical model” section) for the total TOT values at four fixed thresholds for the time distribution spectra calculated by using Eq. 3. In framework of J-PET, the light signals are collected on both sides of plastic scintillator as a measure of energy deposition, so in calculating the TOT_{model} , we used twice the value of TOT_{sum} and the value of free parameter N_0 is 1.3

in Fig. 11b. The black rectangles are the experimental data. Errors in estimating the mean value of the TOT are within the size of the used symbols. It is shown that the used functions (see the caption of Fig. 11) are able to reproduce the data for quite a large range of energy deposition, i.e., up to 1000 keV. The experimental data is confronted also with a theoretical model (the “Theoretical model” section) which well describes the data.

Conclusions

J-PET is the first PET scanner composed of plastic scintillators [3, 30]. Plastic scintillators are more than an order of magnitude less expensive than crystal scintillators. The

time-over-threshold approach facilitates a compact, fast, and cost-effective signal readout [32, 42, 43]. In the framework of J-PET scanner, we adopt the TOT approach as a measure of the energy deposition in order to utilize the fast timing and low pile-up features of the plastics scintillators. To apply this method effectively, in comparison to the classical method of charge collection, it is important to precisely describe the non-linear relationship between the energy deposition of an initial photon and the measured TOT values. Here, we presented a method for determining this relation which we showed can be efficiently applied to the J-PET tomograph by collecting the data with a ^{22}Na source covered with the porous material characterized with the long lifetime of positronium atoms [29]. The identification of an incident photon was based on the angular correlation between the three hits and the lifetime of the metastable positronium atoms while the scattered photon was identified and associated to the initial photon based on the correlation among the registration time and distance between the interaction points. Using a ^{22}Na source emitting 1275 keV prompt and 511 keV annihilation photons, the TOT versus energy loss relationship up to about 1000 keV was established. The proposed functions fits the experimental data well and can be used as a standalone functions for the energy loss calibration of the plastic scintillators used in the J-PET scanner. Furthermore, we also introduced a theoretical model following a simple algorithm able to reproduce the experimental data which may be used in other experimental facilities using the plastic scintillators.

Acknowledgements

The authors acknowledge technical and administrative support of A. Heczko, M. Kajetanowicz, and W. Migdał.

Authors' contributions

All authors contributed in the elaboration of methods for data analysis, interpretation of results, experimental set-up and data collection, correction of manuscript, and approval. The analysis algorithm was mainly developed by SS along with the PM. SS and PM edited the manuscript. All authors read and approved the final manuscript.

Funding

This work was supported by The Polish National Center for Research and Development through grant INNOTECH-K1/IN1/64/159174/NCBR/12, the Foundation for Polish Science through the MPD and TEAM PIOR.04.04.00-00-4204/17, the National Science Centre of Poland through grants no. 2016/21/B/ST2/01222, 2017/25/N/NZ1/00861, the Ministry for Science and Higher Education through grants no. 6673/IA/SP/2016, 7150/E-338/SPUB/2017/1, 7150/E-338/M/2017, 7150/E-338/M/2018, and the Austrian Science Fund FWF-P26783-N27.

Availability of data and materials

The data that support the findings of this study are available from the corresponding author upon request.

Ethics approval and consent to participate

Not applicable

Consent for publication

Not applicable

Competing interests

The authors declare that they have no competing interests

Author details

¹Faculty of Physics, Astronomy and Applied Computer Science, Jagiellonian University, prof. Stanisława Łojasiewicza 11, 30-348 Cracow, Poland. ²INFN, Laboratori Nazionali di Frascati, 00044 Frascati, Italy. ³Institute of Nuclear Physics PAN, Cracow, Poland. ⁴Institute of Physics, Maria Curie-Skłodowska University, 20-031 Lublin, Poland. ⁵Faculty of Physics, University of Vienna, 1090 Vienna, Austria. ⁶Department of Complex Systems, National Centre for Nuclear Research, 05-400 Otwock-Świerk, Poland. ⁷High Energy Physics Division, National Centre for Nuclear Research, 05-400 Otwock-Świerk, Poland. ⁸2nd Department of General Surgery, Jagiellonian University Medical College, Cracow, Poland. ⁹Department of Physics, College of Education for Pure Sciences, University of Mosul, Mosul, Iraq.

Received: 19 November 2019 Accepted: 17 May 2020

Published online: 05 June 2020

References

1. Nygren DR. Converting vice to virtue: can time-walk be used as a measure of deposited charge in silicon detectors?. Intern LBL Note. 1991.

2. Kipnis I, Collins T, DeWitt J, Dow S, Frey A, Grillo A, et al. A time-over-threshold machine: the readout integrated circuit for the BABAR Silicon Vertex Tracker. *IEEE Trans Nucl Sci.* 1997;44(3 PART 1):289–97.
3. Moskal P, Rundel O, Alfs D, Bednarski T, Białas P, Czerwiński E, et al. Time resolution of the plastic scintillator strips with matrix photomultiplier readout for J-PET tomograph. *Phys Med Biol.* 2016;61(5):2025–47.
4. Moskal P, Krawczyk N, Hiesmayr BC, Bala M, Curceanu C, Czerwiński E, et al. Feasibility studies of the polarization of photons beyond the optical wavelength regime with the J-PET detector. *Eur Phys J C.* 2018;78:970.
5. Saint Gobain Crystals. <https://www.crystals.saint-gobain.com/>.
6. Wieczorek A, Dulski AK, Niedzwiecki S, Alfs D, Białas P, Curceanu C, et al. Novel scintillating material 2-(4-styrylphenyl)benzoxazole for the fully digital and MRI compatible J-PET tomograph based on plastic scintillators. *PLoS One.* 2017;12(11):e0186728.
7. Vilardi I, Braem A, Chesi E, Ciocia F, Colonna N, Corsi F, et al. Optimization of the effective light attenuation length of YAP:Ce and LYSO:Ce crystals for a novel geometrical PET concept. *Nucl Instr Meth A.* 2006;564:506–14.
8. Mao R, Zhang L, Ren-Yuan Z. Optical and scintillation properties of inorganic scintillators in high energy physics. *IEEE Trans Nucl Sci.* 2008;55:2425–31.
9. Lanthanum Bromide Properties. <https://www.crystals.saint-gobain.com/products/standard-and-enhanced-lanthanum-bromide>.
10. Olcott PD, Levin CS. Pulse width modulation: a novel readout scheme for high energy photon detection. *IEEE Nucl Sci Symp Conf Rec.* 2008. <https://doi.org/10.1109/nssmic.2008.4774297>.
11. Fujiwara T, Takahashi H, Shimazoe K, Shi B. Multi-level time-over-threshold method for energy resolving multi-channel systems. *IEEE Trans Nucl Sci.* 2010;57(5):2545–8. <https://doi.org/10.1109/tns.2010.2061236>.
12. Orita T, Koyama A, Yoshino M, Kamada K, Yoshikawa A, Shimazoe K, et al. The current mode time-over-threshold ASIC for a MPPC module in a TOF-PET system. *Nucl Inst Methods Phys Res Sect A Accelerators Spectrometers Detectors Associated Equipment.* 2018;912:303–8.
13. Kim H, Kao CM, Xie Q, Chen CT, Zhou L, Tang F, et al. A multi-threshold sampling method for TOF-PET signal processing. *Nuclear Instruments and Methods in Physics Research, Section A: Accelerators, Spectrometers, Detectors and Associated Equipment.* 2009;602(2):618–21.
14. Grant AM, Levin CS. A new dual threshold time-over-threshold circuit for fast timing in PET. *Phys Med Biol.* 2014;59(13):3421–30.
15. Shimazoe K, Takahashi H, Shi B, Orita T, Furumiya T, Ooi J, et al. Dynamic time over threshold method. *IEEE Trans Nucl Sci.* 2012;59(6):3213–7.
16. Orita T, Shimazoe K, Takahashi H. The dynamic time-over-threshold method for multi-channel APD based gamma-ray detectors. *Nucl Inst Methods Phys Res Sect A Accelerators Spectrometers Detectors Associated Equipment.* 2015;775:154–61.
17. Vandenberghe S, Mikhaylova E, D'Hoe E, Mollet P, Karp JS. Recent developments in time-of-flight PET. *EJNM Phys.* 2016;3:1–30.
18. Slomka PJ, Pan T, Germano G. Recent advances and future progress in PET instrumentation. *Semin Nucl Med.* 2016;46:5–19.
19. Vandenberghe S, Moskal P, Karp JS. State of the art in total body PET. *EJNM Phys.* 2020;7:35.
20. Jin-Jie W, Yue-Kun H, Zhi-Jia S, Chong W, Yu-Da Z, Gui-An Y, et al. A study of time over threshold (TOT) technique for plastic scintillator counter. *Chin Physics C.* 2008;32(3):186–90.
21. Ashrafi S, Ghahremani GM. Energy calibration of thin plastic scintillators using Compton scattered γ rays. *Nucl Inst Methods Phys Res Sect A Accelerators Spectrometers Detectors Associated Equipment.* 2011;642(1):70–4.
22. Kowalski P, Wiślicki W, Raczyński L, Alfs D, Bednarski T, Białas P, et al. Scatter fraction of the J-PET tomography scanner. *Acta Physica Polonica B.* 2016;47:549–60.
23. Kowalski P, Wiślicki W, Shopa RY, Raczyński L, Klimaszewski K, Curceanu C, et al. Estimating the NEMA characteristics of the J-PET tomograph using the GATE package. *Phys Med Biol.* 2018;63(16):165008–165025.
24. Compton HA. The spectrum of scattered x-rays. *Phys Rev.* 1923;22(20):2–6.
25. Garwin RL. Thermalization of positrons in metals. *Phys Rev.* 1953;91:1571–2.
26. Moskal P, Kisiulewska D, Curceanu C, Czerwiński E, Dulski K, Gajos A, et al. Feasibility study of the positronium imaging with the J-PET tomograph. *Phys Med Biol.* 2019;64(5):055017.
27. Moskal P, Jasińska B, Stępień E Ł., Bass S. Positronium in Medicine and Biology. *Nat Rev Phys.* 2019;1:527–9. <https://doi.org/10.1038/s42254-019-0078-7>.
28. Dulski K, Curceanu C, Czerwiński E, Gajos A. Commissioning of the J-PET detector in view of the positron annihilation lifetime spectroscopy. *Hyperfine Interactions.* 2018;239(40):1–6.
29. Jasińska B, Gorgol M, Wiertel M, Zaleski R, Alfs D, Bednarski T, et al. Determination of the 3γ fraction from positron annihilation in mesoporous materials for symmetry violation experiment with J-PET scanner. *Acta Physica Polonica B.* 2016;47(2):453–60.
30. Niedzwiecki S, Białas P, Curceanu C, Czerwiński E, Dulski K, Gajos A, et al. J-PET: a new technology for the whole-body PET imaging. *Acta Phys Polon B.* 2017;48(10):1567–76.
31. Raczyński L, Moskal P, Kowalski P, Wiślicki W, Bednarski T, Bia P, et al. Compressive sensing of signals generated in plastic scintillators in a novel J-PET instrument. *Nucl Inst Methods Phys Res Sect A Accelerators Spectrometers Detectors Associated Equipment.* 2015;786:105–12.
32. Pałka M, Strzempke P, Korcyl G, Bednarski T, Niedzwiecki S, Białas P, et al. Multichannel FPGA based MVT system for high precision time (20 ps RMS) and charge measurement. *J Instrum.* 2017;12:P08001.
33. Raczyński L, Moskal P, Kowalski P, Wiślicki W, Bednarski T, Białas P, et al. Novel method for hit-position reconstruction using voltage signals in plastic scintillators and its application to positron emission tomography. *Nucl Inst Methods Phys Res Sect A Accelerators Spectrometers Detectors Associated Equipment.* 2014;764:186–92.
34. Moskal P, Niedzwiecki S, Bednarski T, Czerwiński E, Kapłon, Kubicz E, et al. Test of a single module of the J-PET scanner based on plastic scintillators. *Nucl Inst Methods Phys Res Sect A Accelerators Spectrometers Detectors Associated Equipment.* 2014;764:317–21.

35. Sharma NG, Silarski M, Bednarski T, Białas P, Czerwiński E, Gajos A, et al. Reconstruction of hit time and hit position of annihilation quanta in the J-PET detector using the Mahalanobis distance. *Nukleonika*. 2015;60(4):765–9.
36. Won JY, Lee JS. Highly integrated FPGA-only signal digitization method using single-ended memory interface input receivers for time-of-flight PET detectors. *IEEE Trans Biomed Circ Syst*. 2018;2865581:1–10.
37. Won JY, Kwon SI, Yoon HS, Ko GB, Son JW, Lee JS. Dual-phase tapped-delay-line time-to-digital converter with on-the-fly calibration implemented in 40 nm FPGA. *IEEE Trans Biomed Circ Syst*. 2016;10:231–42.
38. Won JY, Lee JS. Time-to-digital converter using a tuned-delay line evaluated in 28-, 40-, and 45-nm FPGAs. *IEEE Trans Instrum Meas*. 2016;65:1678–89.
39. Palka M, Moskal P, Bednarski T, Białas P, Czerwiński E, Kaplon Ł, et al. A novel method based solely on field programmable gate array (FPGA) units enabling measurement of time and charge of analog signals in positron emission tomography (PET). *BioAlgoritm MedSyst*. 2014;10:41–5.
40. Kim H, Kao CM, Xie Q, Chen CT, Zhou L, Tang F, et al. A multi-threshold sampling method for TOF-PET signal processing. *Nucl Instr and Meth A*. 2009;602:618–21.
41. Xi D, Zheng C, Liu W, Liu X, Wan L, Kim H, et al. A PET detector module using FPGA-only MVT digitizers. *Nucl Sci Symp Med Imaging Conf (NSS/MIC) IEEE*. 2013;10:1–5.
42. Korcyl G, Alfs D, Bednarski T, Białas P, Czerwiński E, Dulski K, et al. Sampling FEE and trigger-less DAQ for the J-PET scanner. *Acta Phys Pol B*. 2016;47(2):491–6.
43. Korcyl G, Białas P, Curceanu C, Czerwiński E, Hiesmayr BC, Jasi B, et al. Evaluation of single-chip, real-time tomographic data processing on FPGA SoC devices. *IEEE Trans Med Imaging*. 2018;37(11):2526–35.
44. Pawlik-Niedźwiecka M, Niedźwiecki S, Białas P, Curceanu C, Czerwiński E, Dulski K, et al. Preliminary studies of J-PET detector spatial resolution. *Acta Phys Polon A*. 2017;132(5):1645–8.
45. Lecoq P, Auffray E, Brunner S, Hillemanns H, Jarron P, Knapitsch A, et al. Factors influencing time resolution of scintillators and ways to improve them. *IEEE Trans Nucl Sci*. 2010;57(5):2411–6.
46. Krzemień W, Bala M, Bednarski T, Białas P, Czerwiński E, Gajos A, et al. Processing optimization with parallel computing for the J-PET scanner. *Nukleonika*. 2015;60(4):745–8.
47. Krzemień W, Alfs D, Białas P, Czerwiński E, Gajos A, Glowacz B, et al. Overview of the software architecture and data flow for the J-PET tomography device. *Acta Phys Polon B*. 2016;47(2):561–7.
48. Kamińska D, Gajos A, Czerwiński E, Alfs D, Bednarski T, Białas P, et al. A feasibility study of ortho-positronium decays measurement with the J-PET scanner based on plastic scintillators. *Eur Phys J C*. 2016;76(445):1–14.
49. Czerwiński E, Dulski K, Białas P, Curceanu C, Czerwiński E, Dulski K, et al. Commissioning of the J-PET detector for studies of decays of positronium atoms. *Acta Phys Polon B*. 2017;48(10):1961–8.
50. Moszyński M, Bengtson B. Light pulse shapes from plastic scintillators. *Nucl Inst Methods*. 1977;142:417–34.
51. Moszyński M, Bengtson B. Status of timing with plastic scintillation detectors. *Nucl Inst Methods*. 1979;158:1–31.

Publisher's Note

Springer Nature remains neutral with regard to jurisdictional claims in published maps and institutional affiliations.

Submit your manuscript to a SpringerOpen[®] journal and benefit from:

- Convenient online submission
- Rigorous peer review
- Open access: articles freely available online
- High visibility within the field
- Retaining the copyright to your article

Submit your next manuscript at ► [springeropen.com](https://www.springeropen.com)